Materials Today Bio 12 (2021) 100137

Contents lists available at ScienceDirect

Materials Today Bio

journal homepage: www.journals.elsevier.com/materials-today-bio

Maturation of biomimetic hydroxyapatite in physiological fluids: a physicochemical and proteomic study

J. Konka [a,b], M. Espanol [a,b], B.M. Bosch [c], E. de Oliveira [d], M.-P. Ginebra [a,b,e,*]

[a] Biomaterials, Biomechanics and Tissue Engineering Group, Department of Materials Science and Engineering, Universitat Politècnica de Catalunya (UPC), Av. Eduard Maristany 16, 08019, Barcelona, Spain
[b] Barcelona Research Center in Multiscale Science and Engineering, Universitat Politècnica de Catalunya (UPC), Av. Eduard Maristany 16, 08019, Barcelona, Spain
[c] Bioengineering Institute of Technology (BIT), Universitat Internacional de Catalunya (UIC), Josep Trueta s/n, 08195, Barcelona, Spain
[d] Plataforma de Proteòmica, Parc Científic de Barcelona, PCB, Barcelona, Spain
[e] Institute for Bioengineering of Catalonia (IBEC), The Barcelona Institute of Science and Technology, Baldiri Reixac 10-12, 08028, Barcelona, Spain

ARTICLE INFO

Keywords:
Calcium phosphates
Protein adsorption
Nanostructure
Raman spectroscopy
Ion exchange

ABSTRACT

Biomimetic calcium-deficient hydroxyapatite (CDHA) as a bioactive material exhibits exceptional intrinsic osteoinductive and osteogenic properties because of its nanostructure and composition, which promote a favorable microenvironment. Its high reactivity has been hypothesized to play a relevant role in the *in vivo* performance, mediated by the interaction with the biological fluids, which is amplified by its high specific surface area. Paradoxically, this high reactivity is also behind the *in vitro* cytotoxicity of this material, especially pronounced in static conditions. The present work explores the structural and physicochemical changes that CDHA undergoes in contact with physiological fluids and to investigate its interaction with proteins. Calcium-deficient hydroxyapatite discs with different micro/nanostructures, coarse (C) and fine (F), were exposed to cell-free complete culture medium over extended periods of time: 1, 7, 14, 21, 28, and 50 days. Precipitate formation was not observed in any of the materials in contact with the physiological fluid, which would indicate that the ionic exchanges were linked to incorporation into the crystal structure of CDHA or in the hydrated layer. In fact, CDHA experienced a maturation process, with a progressive increase in crystallinity and the Ca/P ratio, accompanied by an uptake of Mg and a B-type carbonation process, with a gradual propagation into the core of the samples. However, the reactivity of biomimetic hydroxyapatite was highly dependent on the specific surface area and was amplified in nanosized needle-like crystal structures (F), whereas in coarse specimens the ionic exchanges were restricted to the surface, with low penetration in the material bulk. In addition to showing a higher protein adsorption on F substrates, the proteomics study revealed the existence of protein selectivity toward F or C microstructures, as well as the capability of CDHA, and more remarkably of F-CDHA, to concentrate specific proteins from the culture medium. Finally, a substantial improvement in the material's ability to support cell proliferation was observed after the CDHA maturation process.

1. Introduction

In the last decades, various synthetic bone grafting strategies have been designed to meet the increasing demand in the aging society as an alternative to autografts. Different materials have been proposed over the years, including calcium sulfates, bioactive glasses, and calcium phosphate (CaP) ceramics and cements [1,2]. Calcium phosphate have positioned themselves as particularly attractive owing to the excellent biocompatibility and the similarity of their composition and structure to natural bones [3–5]. An especially outstanding *in vivo* performance has been recently demonstrated by biomimetic calcium deficient hydroxyapatite (CDHA) synthesized at low temperatures, which has proven to outperform the traditional sintered calcium phosphates in terms of osteoinduction and osteogenic potential, in addition to showing a good synchronization between biomaterial resorption and bone formation [6–8]. The nanostructure and, linked to it, the high specific surface area proved to be a key factor in this behavior generating a favorable osteoimmune environment for osteoblast differentiation and osteogenesis *in vitro* [9] and promoting ectopic bone formation *in vivo* [8]. The high reactivity of CDHA, associated to both its chemical composition and

* Corresponding author.
E-mail address: maria.pau.ginebra@upc.edu (M.-P. Ginebra).

https://doi.org/10.1016/j.mtbio.2021.100137
Received 23 June 2021; Received in revised form 20 August 2021; Accepted 4 September 2021
Available online 15 September 2021

textural properties, has been hypothesized to play a relevant role in the *in vivo* performance, mediated by the interaction of the material with the biological fluids, which in this material is amplified by its high specific surface area. In particular, there are two relevant phenomena in this interaction, namely ionic exchange and protein adsorption.

Ionic exchange has been associated to many of the biological responses elicited by biomaterials after implantation, such as mineralization, bioactivity, osteogenesis, or osteoinduction [4,10–12]. This is not limited to the obvious release of calcium and phosphorus when a calcium phosphate material is degraded. In the case of CDHA, it is known that when it comes into contact with physiological fluids ion exchange takes place, with a significant uptake of calcium. This has been extensively documented in *in vitro* studies, and in fact the high ionic fluctuations in static conditions have been associated to the *in vitro* cytotoxicity of this material [13–16], a problem that can be overcome doing dynamic cultures using microfluidic-based strategies [17].

The reason for the drastic ionic exchanges in CDHA, and in general in any nanoapatite, has been hypothesized to be associated to the so-called maturation process that poorly crystalline materials undergo toward more crystalline and stable crystals [18–22]. This would mean that as a result of the interaction with the body fluids the material would undergo a progressive evolution toward a more stable apatitic phase. However, up to now this has not been demonstrated. The attention has been focused in the evolution of the ionic fluctuations triggered by CDHA, for instance the cell culture media, and their consequences for the *in vitro* cell behavior [16,23,24] rather than trying to understand the natural evolution of CDHA in contact with the physiological fluids.

Regarding protein adsorption, this is known to be the second event after the implantation of any material in the human body, preceded by adsorption of water molecules [25], which further influences the behavior of cells and determines the response to tissue regeneration [26]. Like the maturation process, this is a dynamic process as the nature of the adsorbed protein layer will change with time, leading to a progressive enrichment of the proteins with high affinity for the biomaterial (Vroman effect [27–29]). Understanding the composition of the adsorbed protein layer is key as this will determine cell adhesion, cell growth, cell differentiation, and formation of the extracellular matrix [30]. For example, the osteoinductive capacity of a biomaterial has been hypothesized to be linked to the initial protein adsorption [4,11,31]. Despite the importance in understanding the nature of proteins adsorbed on the surface of biomaterials, many of the available methods used to investigate protein adsorption such as western blotting, radiolabeling [32], optical ellipsometry [33], surface plasmon resonance [34], total internal reflection fluorescence [35], or FTIR/ATR [36,37] allow investigating individual or a small number of proteins and therefore cannot be used to analyze the entire mix of proteins adsorbed from serum. To circumvent this problem, proteomics analyses using liquid chromatography–mass spectrometry (LC-MS/MS) emerge as a powerful alternative by allowing to determine simultaneously the identity and concentration of complex protein mixtures [38]. Recently, its use in protein adsorption on biomaterial surfaces has sparked the interest of scientists [39]. However, in the field of bone regeneration, investigation of protein adsorption by LC-MS/MS on synthetic bone grafts are still scarce. Kaneko et al. (2011) [40] compared the behavior of sintered hydroxyapatite (sHA) and octacalcium phosphate (OCP) in contact with rat blood serum where higher number of proteins were adsorbed on the OCP with larger specific surface area (SSA). Interestingly, they observed that bone-related proteins were more attracted to sHA than to OCP. In a study by Othman et al. (2020) [41], sHA, and β-tricalcium phosphate (β-TCP) were incubated in the osteogenic cell culture medium where again protein adsorption was highly influenced by the SSA of the compared materials, i.e. a higher number of adsorbed proteins were observed for β-TCP, which exhibited greater SSA. In addition, the study showed that, among the common proteins adsorbed on both materials, some were more abundant in HA despite its lower SSA, probing protein selectivity. Romero-Gavilan et al. (2017) [42], in their study of protein adsorption on four types of sol–gel biomaterials based on silicates for dental applications, have put forward an interesting idea that a proteomic analysis could serve as a better alternative to standard *in vitro* testing for predicting performance *in vivo* according to their analyses. The possibility of profiling complex protein mixtures and identifying differences in protein adsorption is a powerful tool that can help understanding which biological processes would be favored in subsequent stages of bone regeneration and may prove to be a key tool in determining *in vivo* potential of a biomaterial.

The present work explores the changes that CDHA undergoes in contact with physiological fluids and to investigate its interaction with proteins. To this aim the maturation of CDHA in serum supplemented culture medium was monitored over extended incubation times up to 50 days. To accelerate maturation the culture medium was exchanged daily. The maturation of two biomimetic CDHA with different micro/nanostructures was compared, plate-like and needle-like, with the latter having double SSA. Regarding proteomics analysis, triplicate analyses were done on both substrates after 7 days incubation in the culture medium to decipher the adsorption profile of fetal bovine serum proteins supplemented in the cell culture medium.

2. Materials and methods

2.1. Material preparation

Biomimetic hydroxyapatite was obtained by a self-setting reaction based on the hydrolysis of α-tricalcium phosphate (α-TCP) paste at 37 °C as described previously [43]. Alpha-tricalcium phosphate was fabricated by sintering a mixture of $CaHPO_4$ (Sigma Aldrich, St. Louis, USA) and $CaCO_3$ (Sigma Aldrich, St. Louis, USA) in a Ca/P ratio 1.5 at 1400 °C for 15 h and was subsequently rapidly quenched to room temperature. Two milling protocols were used to obtain (i) coarse (C; median particle size 10.2 μm) and (ii) fine (F; median particle size 4.02 μm) [44] α-TCP powder. To obtain moldable pastes, the coarse or fine α-TCP powders were mixed with distilled H_2O using a liquid to powder ratio of 0.5 mL/g. The paste was then put into Teflon® molds to obtain 5.5 mm diameter x 2 mm height discs and pre-set 24 h in 100% relative humidity. Afterward, the discs were immersed in distilled H_2O at 37 °C for 10 days to allow the full transformation of α-TCP to CDHA.

2.2. Incubation in serum supplemented culture medium

The $CDHA_F$ and $CDHA_C$ discs were sterilized in 70% ethanol and then washed thrice with phosphate buffered saline (PBS). Afterwards, the discs were distributed in 24-well plates. The samples were incubated in Advanced Dulbecco's Modified Eagle's Medium (AdvDMEM) supplemented with 10% fetal bovine serum (FBS), 2 mM L-glutamine, penicillin/streptomycin (50 U/ml and 50 μg/mL, respectively) and 20 mM HEPES buffer – all from Invitrogen (from hereon called *complete* AdvDMEM) for 1, 7, 14, 21, 28 and 50 days. For incubation of each sample, 2 mL of the culture medium was used and changed daily. For each time point, three discs were incubated independently. After collection, all specimens were washed thrice in 100 mL distilled H_2O for 5 min to ensure the elimination of superficial residues on the samples.

2.3. Evolution of CDHA

2.3.1. Textural properties

The specific surface area (SSA) was determined by nitrogen sorption using the Brunauer- Emmett-Teller method (ASAP 2020, Micromeritics, USA). Prior to the measurements, the samples were outgassed at 10 mmHg at a holding temperature of 100 °C for 2 h in vacuum conditions.

Mercury intrusion porosimetry (MIP, AutoPore IV, Micromeritics, USA) was carried out to characterize the open porosity and pore entrance size distribution.

2.3.2. Microstructural evolution

The microstructure of the surface and the cross-section of the specimens after different immersion periods was characterized by scanning electron microscopy (SEM, Zeiss Neon 40) with an acceleration voltage of 5 kV. The analyzed surface was coated with carbon using EMITECH K950X.

2.3.3. Grazing incidence X-ray diffraction (GIXRD) and confocal Raman microscopy (CRM)

The surface phase composition was assessed by grazing incidence X-ray diffraction (XRD) using a D8 Advance diffractometer (Bruker, USA). Scanning was performed in the Bragg–Brentano geometry using Cu Kα radiation with the following conditions: 2θ scan range of 10–80°, with a scan step of 0.02°, and a counting time of 2 s per step at 40 kV and 40 mA with the grazing angle set at 1°. The crystallite size was calculated using the Scherrer's equation on the (002) diffraction peak as follows:

$$X_{hkl} = K \cdot \frac{\lambda}{\beta_{1/2} \cos\theta}$$

where X_{hkl} is the crystallite size (nm), λ is the wavelength of monochromatic X-ray beam (nm) (0.15406 nm for Cu K radiation), $\beta_{1/2}$ is the full width at half maximum for the diffraction peak under consideration (rad), θ is the diffraction angle (in degrees), and K is a constant varying with crystal habit and hereon set to 0.9.

Confocal Raman microscopy (inVia™ Qontor® confocal Raman microscope, Renishaw Inc.) was used to assess the chemical changes in the CDHA discs over extended incubation times in culture medium. Two type of measurements (a) triplicate single point measurements on the surfaces of the discs and (b) mapping measurements of the polished cross-sections incubated over 0, 21, and 50 days were carried out. Mappings were performed on the cross-sections from the surface to the interior part of discs. The area mapped for each specimen was 90 μm × 500 μm, with 10 μm resolution. The Raman spectra were obtained using ×50 L (long working distance) objective and either (i) 785 nm laser source with 1200 L/mm (vis) grating, 150 mW laser power, 1 s or 0.1 s exposure time, and 20 or 25 accumulations for point and mapping measurements respectively, using static mode with Raman shift center at 1000 cm^{-1} with spectral resolution of 1.2 cm^{-1}; or (ii) 532 nm laser source with 2400 L/mm (vis) grating, 50 mW laser power, 0.5 s or 0.1 s exposure time, and 20 or 25 accumulations for point and mapping measurements respectively, using static mode with Raman shift center at 3300 cm^{-1} with spectral resolution of 0.8 cm^{-1}. For the mappings, two replicates at 50 days of incubation were measured, to assess the reproducibility of the results. The spectra collected were analyzed with WiRE 4.4 software.

2.3.4. ICP-OES – elemental analysis

Inductively coupled plasma through optical emission spectroscopy (ICP-OES, Agilent 5100/5110 VDV; SPS4 Autosampler, Agilent Technologies, Japan) was used to perform elemental analysis of both the supernatants of the culture medium in contact with the CDHA discs and the digested discs themselves. For the latter, the discs from each time point were broken in halves, and one of them was lightly ground in an agate mortar. Subsequently, these powders were put in Eppendorfs and washed by immersion in 1 mL of distilled H_2O for 30 min. Then the water was removed, and the samples were lyophilized (Cryodos 80, Telstar), digested in 20% HNO_3 (69% HNO_3 for analysis, PanReac AppliChem, ITW Reagents) and diluted to 1:80 with miliQ water obtaining 2% HNO_3 final solution. In turn, the supernatants were diluted 1:10 in a solution of 2% HNO_3. The presence of elements, such as Ca, P, and Mg ions, was determined. ^{44}Ca, ^{31}P, and ^{25}Mg signals were calibrated against a custom-made multi-element standard solution (Inorganic Ventures, USA).

2.3.5. Proteomics

The proteomics work was done at the Proteomics Platform of Barcelona Science Park, a member of ProteoRed-ISCIII. Liquid chromatography and tandem mass spectrometry (LC-MS/MS) was used to analyze protein adsorption on C and F discs surfaces after incubation over 7 days in complete AdvDMEM (n = 3) (CM). The protein content of the cell culture medium was analyzed as control (n = 2).

Three replicate samples (C and F) and duplicate samples of CM control were enzymatically digested as follows. Briefly, proteins were reduced with dithiothreitol (20 mM in NH_4HCO_3; over 60 min at 60 °C) and alkylation (iodoacetamide 55 mM in NH_4HCO_3; at 25 °C over 30 min in the dark). Afterward, the samples were twice digested (2 h and overnight) with Trypsin at 37 °C (sequence grade modified Trypsin, Promega). The extraction of the resulting peptide mixtures from the discs was done with 5% formic acid (FA) in 50% ACN, and 100% ACN, and then were dried-down in a SpeedVac vacuum system to reduce their volume. Subsequently, the peptides were desalted with C18 tips (P200 top tip, PolyLC Inc.), following the manufacturer's manual, and dried-down using a SpeedVac vacuum system. The dried-down peptide mixtures were analyzed in a nanoAcquity liquid chromatographer (Waters) coupled to an LTQ-Orbitrap Velos (Thermo Scientific) mass spectrometer.

The raw data files obtained in the mass spectrometry analyses were used to search against the public database UniProt containing all *Bos Taurus* protein entries (v. 21/5/19). Database search was performed with Mascot search engine (v. 2.3.1) using Proteome Discoverer (v. 1.4). For each identified protein an exponentially modified protein abundance index (emPAI) defined as 10^{PAI} -1, where PAI is the number of experimentally observed peptides divided by the calculated number of observable peptides for each protein was calculated and used as a semi-quantitative method for estimating relative protein amount in the tested samples [45–47]. Principal component analysis (PCA) on triplicate (C and F) and duplicate (CM) emPAI results was performed using python scikit-learn library (https://scikit-learn.org). The UniProtKB database served to obtain molecular weights of the detected proteins. Biological functions search of bone regeneration important proteins was performed using the DAVID bioinformatics database (www.david.ncifcrf.gov), STRING database (https://string-db.org/), and literature review. The proteins detected in all replicate samples were classified by Gene Ontology (GO) and Reactome pathway using the STRING database (https://string-db.org/), and further the groups of proteins taking part in the regulation of ERK1 and ERK2 cascade, complement activation, bone resorption, regulation of bone mineralization, fibrinogen complex, formation of fibrin clot (clotting cascade), and regulation of complement cascade were correlated with the results of emPAI.

2.4. In vitro response of human mesenchymal stem cells (hMSCs) to matured CDHA

To assess the effect of the maturation of biomimetic CDHA exposed to body fluids on cell interaction, human mesenchymal stem cells (hMSCs) were cultured on C and F CDHA discs (5.5 mm diameter), either pristine or after 40 days incubation in cell culture medium (section 2.2). Previously, the hMSCs were expanded in AdvDMEM supplemented with 10% fetal bovine serum (FBS), 2 mM L-glutamine, 50 U ml^{-1} penicillin, and 50 mg mL^{-1} streptomycin (all from Invitrogen, USA). The discs were sterilized by gamma rays at 8 kGy, placed in a low-attachment 24-well plate, and further preconditioned over 48 h in cell culture media. As a control, tissue culture polystyrene (TCPS) was used. For all the experiments, hMSCs at passage 5 were seeded at a density of 300 cells/mm^2 and were allowed to attach at 37 °C and 5% CO_2. Thereafter, hMSCs were incubated on the samples and extracted for further analysis after 6 h, 3 days, and 14 days, renewing the medium (2 mL) every day. At each specified time point, discs were transferred to a new 24-well plate to discard attached cells at the bottom of the well plate, washed thrice with PBS, and lysed with 900 μL M-PER® (Mammalian Protein Extraction Reagent, Thermo Scientific, Waltham, MA, USA). The cell number was quantified by Cytotoxicity Detection Kit (Roche Applied Science, Penzberg, Germany) following the manufacturer's protocol. A calibration curve with increasing number of cells was prepared, and LDH activity

was measured at 492 nm with the Synergy HTX multimode microplate reader (Bio-Tek). Results of the LDH number were normalized *versus* the area of the corresponding substrate. Four independent biological replicates were performed.

Cell morphology was characterized by scanning electron microscopy (SEM, JEOLJSM7001F, Japan) with an acceleration voltage of 2 kV (SED) and 5 kV (BSD). Carbon coating was deposited on the surfaces of the samples with the EMITECH K950X vacuum evaporator.

2.5. Statistics

The experiments were performed in independent triplicates unless stated otherwise. The results are shown as a mean ± standard deviation. Statistical analysis of the normally distributed data was performed using either ANOVA with the post-hoc Tukey test or multiple paired *t*-test with the significance level set at *p*-value <0.05. For the proteomics study, a multiple paired *t*-test at a significance level of *p*-value <0.05 with false discovery rate correction using the Benjamin/Hochberg method was performed to compare emPAI values of detected proteins.

3. Results

3.1. Textural properties

The SSA obtained by nitrogen adsorption, the open porosity obtained by MIP, and the apparent density are depicted in Fig. 1A. Fine samples revealed 1.7 times higher SSA than the coarse ones, whereas in case of the open porosity values at 44% and 41% were observed for fine and coarse discs, respectively. A shift to slightly larger entrance pore sizes were observed for fine discs than the coarse ones which showed broader distribution centered at smaller entrance pore sizes (Fig. 1B).

3.2. Microstructural evolution

The microstructure of the surface and the cross-section of the two CDHA substrates, before and after different periods of incubation in complete AdvDMEM is shown in Fig. 2. The typical plate-like and needle-like crystal morphology was exhibited by C and F specimens, respectively, both in the original and in the incubated samples. No additional features in form of newly precipitated crystals or layers were detected in the samples exposed to the culture medium.

3.3. Grazing incidence X-ray diffraction and confocal Raman microscopy

The lack of precipitation of a new crystalline phase on the surfaces of the samples incubated in cell culture media was substantiated by the grazing incidence X-ray diffraction plots shown in Fig. 3A. In the coarse samples, the disappearance of a small amount of α-TCP remaining in the 0 d sample was observed, indicating the completion of the hydrolysis reaction during the first 7 days of incubation. Coarse CDHA was more crystalline already at 0 h of incubation than fine CDHA, and only a slight increase in the crystallinity was observed in the following 7, 14, and 28 days. In contrast, in fine CDHA the peaks became sharper at increasing incubation times, especially noticeable for the reflections corresponding to (112), (211), and (300) crystal planes of hydroxyapatite. This was confirmed by the crystallite sizes calculated using Scherrer's formula for (002) crystal plane (Table 1), which indicated an increase in the crystallinity and consequently, a maturation of CDHA with incubation in the culture medium.

The Raman spectra of the surface of the specimens after different immersion times are shown in Fig. 3B, where the characteristic phosphate bands for synthetic hydroxyapatite can be observed. The doubly degenerate bending O–P–O (ν_2) at 430 and 446 cm^{-1}, the triply degenerate bending O–P–O (ν_4) at 579, 590, and 607 cm^{-1}, the non-degenerate symmetric stretching P–O (ν_1) at 962 cm^{-1} and the triply degenerate asymmetric stretching P–O (ν_3) at 1029, 1046, and 1080 cm^{-1} [48–51]. Furthermore, the P–OH stretching vibration at 873 cm^{-1} and at 1003 cm^{-1} both assigned to HPO_4^{2-} could be observed [49–52]. Thy hydroxyl stretching band [50] at 3750 cm^{-1} could also be appreciated. However, it was only visible for coarse samples up to 28 d of incubation and for fine ones only at 0 h of incubation. The most notable change upon sample incubation, apart from the gradual disappearance of the OH^- band, was detected in the $\nu_3PO_4^{3-}$ region, where an increase in the band between 1070 and 1080 cm^{-1} was observed with incubation time (Fig. 3B). It is known that in apatite the phosphate vibration mode 3 ($\nu_3PO_4^{3-}$) generates three bands at 1029, 1046, and 1080 cm^{-1} which are very close to bands observed for the non-incubated control discs, 1030, 1047, and 1080 cm^{-1}. With the increase in the incubation time, the phosphate band at 1080 cm^{-1} increased in intensity and was shifted to 1072 cm^{-1}. As reported in previous works [48,50,53], those changes are indicative of a B-type carbonate substitution in calcium phosphates where the most intense ν_1 carbonate vibration band ($\nu_1CO_3^{2-}$) superimposes the $\nu_3PO_4^{3-}$ at 1076 cm^{-1}, causing its growth in intensity and shift to lower wavenumbers. Hence, the observable changes were attributed to the carbonation of the apatite over increasing incubation times in the culture medium. An estimation of the degree of carbonation can be made from the ratio between the intensity of the $\nu_1CO_3^{2-}$ band at 1070–1080 cm^{-1} and the neighboring $\nu_3PO_4^{3-}$ band at 1047 cm^{-1}. The amount of carbonate detected on the surface of the CDHA (F and C) discs was found to raise with the incubation time in the complete AdvDMEM as depicted in Fig. 3C. The $\nu_1CO_3^{2-}/\nu_3PO_4^{3-}$ ratio showed increasing carbonation for both surfaces of F and C discs, proving high surface reactivity of CDHA irrespective of the microstructure. A slightly higher carbonation for F specimens at 50 days was observed when compared with the C ones.

On the other hand, Raman mappings of the cross-section of the discs (Fig. 4) showed clear differences in the degree of carbonation depending on the discs' microstructure. That is, the carbonation of C discs was mostly restricted to the underlying surface whereas for the F samples carbonation propagated steadily into the interior part of the specimens. Globally, the fine discs were found to undergo greater rate of carbonation than the

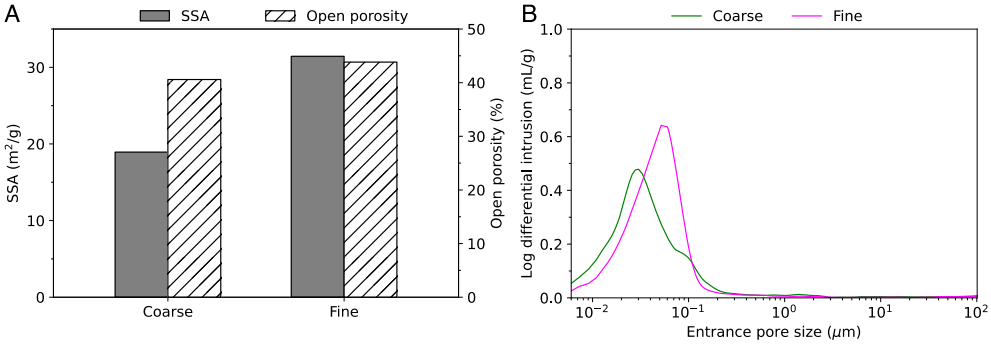

Fig. 1. Specific surface area (SSA) and percentage of open porosity values for coarse and fine discs at 0 h and (B) pore entrance size distributions of coarse and fine specimens at 0 h as determined by MIP.

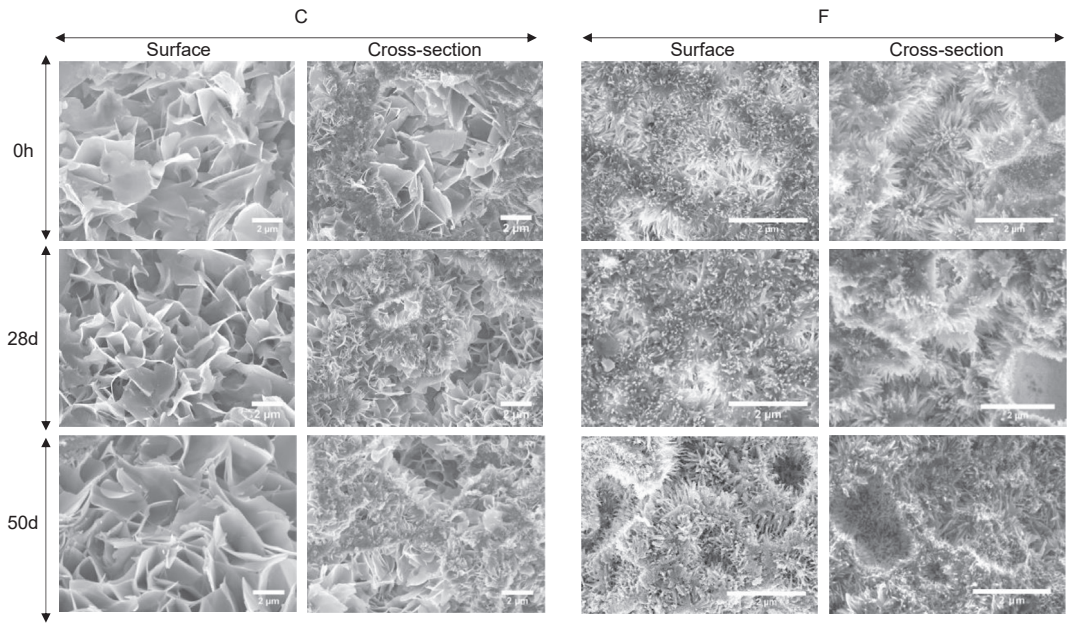

Fig. 2. Morphology of CDHA crystals observed using SEM of coarse (C) and fine (F) discs at 0 h and 28, and 50 day of incubation. On the left view of the crystals on the surface and on the right in the cross-section of the samples for both C and F. Scale bar represents 2 μm. CDHA, calcium-deficient hydroxyapatite; SEM, scanning electron microscopy.

coarse ones. The mapping results of the evolution of the OH^- stretching band in the cross-section of both C and F samples are depicted in Fig. 5. A stronger decrease of the OH^- band was observed for the fine specimens, where at 21 days the peak disappeared across the whole studied area corresponding to a penetration depth of 500 μm. In the case of the coarse samples the decrease in intensity of the hydroxyl group was restricted to the region close to the surface (up to around 60 μm penetration after 50 days incubation), similarly to the carbonation effect observed previously.

3.4. ICP-OES - elemental analysis

The evolution of Ca^{2+}, P_i and Mg^{2+} concentration in the cell culture medium during the incubation of CDHA discs is displayed in Fig. 6A. The initial concentrations of the mentioned ions measured in complete AdvDMEM were respectively 1.82 ± 0.09 mM for Ca^{2+}, 1.17 ± 0.11 mM for P_i, and 0.82 ± 0.04 mM for Mg^{2+}.

For both C and F discs, a clear uptake of Ca was observed which decreased over time. Thus, at day 1 of incubation an abrupt decrease in Ca concentration in the culture medium was observed by as much as 70% for F and 30% for C discs. This uptake was reduced over the course of the incubation to reach 7 and 36% for C and F specimens, respectively, at 21 days. At 50 days, Ca concentration reached the initial values in the culture medium for C discs, whereas for F discs the value was still 22% lower than the initial concentration of Ca.

As far as the changes in P_i concentration are concerned, different trends were observed for F and C discs. Small changes were found for the latter, remaining close to the initial experimental value 1.17 ± 0.11 mM. On the other hand, a stable drop of about 20–25% of P_i concentration was registered for the F specimens for all time points except for day 1, where a sudden increase close to 20% was observed, indicating a release of this ion from the discs.

Similar to the changes in Ca levels in the culture medium, Mg uptake was visible during the first incubation time points for F specimens with a decrease of 46% at day 1 and a tendency to attenuate with time. On the other hand, no changes in Mg concentration were observed for C samples over the duration of the study.

To better understand the relationship between the ionic changes in the liquid medium and their effect on CDHA, the evolution of the same ions was also analyzed upon digestion of the discs. The changes in the Ca/P ratio are displayed in Fig. 6B. The exposure to complete AdvDMEM resulted in a gradual increase of Ca/P ratio for both CDHA samples with incubation time. The changes were however more marked for the F-CDHA, reaching a Ca/P value of around 1.52 at day 50, while in C-CDHA was 1.49. It is worth noting that since these values are obtained digesting the whole disc, any local change on the surface of the discs would be diluted by the contribution of the whole sample. Thus, larger differences than the ones observed are to be expected on the surface of the samples. The Mg atomic % increased 200% by day 50 of incubation for F samples, whereas in case of C substrates Mg concentration incremented linearly up to 25.1% of the initial value at day 50.

3.5. Proteomics

3.5.1. Protein abundance analysis

Proteomic analyses were performed to identify and determine the abundance of proteins adsorbed to C and F discs from the cell culture medium. The number of all identified proteins and their abundance in terms of emPAI count (where emPAI is directly proportional to protein content [54]) obtained for C and F specimens incubated in complete AdvDMEM for 7 days and the culture medium control (CM) are given in Table 2. The statistical analysis was performed comparing the different sample types: C, F, and CM. No statistically significant differences were observed between the number of proteins detected for C and F, nor for F and CM. However, significantly higher number of proteins was identified for C than for CM. As far as the total emPAI count is concerned, significantly higher values were obtained for F specimens than C specimens and CM control.

Principal component analysis (PCA) was performed to detect correlations between protein abundance in the different samples. This analysis helps to reduce the complexity of the study by focusing only on the major differences existing in terms of protein abundance within samples. Thus, the terms principal component 1 and 2 (PC1 and PC2) in Fig. 7A are defined as the first and second largest abundance variability observed from the whole dataset: PC1 accounts for 70.4% of the whole abundance variability while PC2 to 19.1%. The larger the absolute value of the PC component, indicates a strong effect on that PC. What is important from the PCA plot in Fig. 7A, built using the emPAI abundances of all detected proteins with the exception of albumin due to its oversaturation (a total

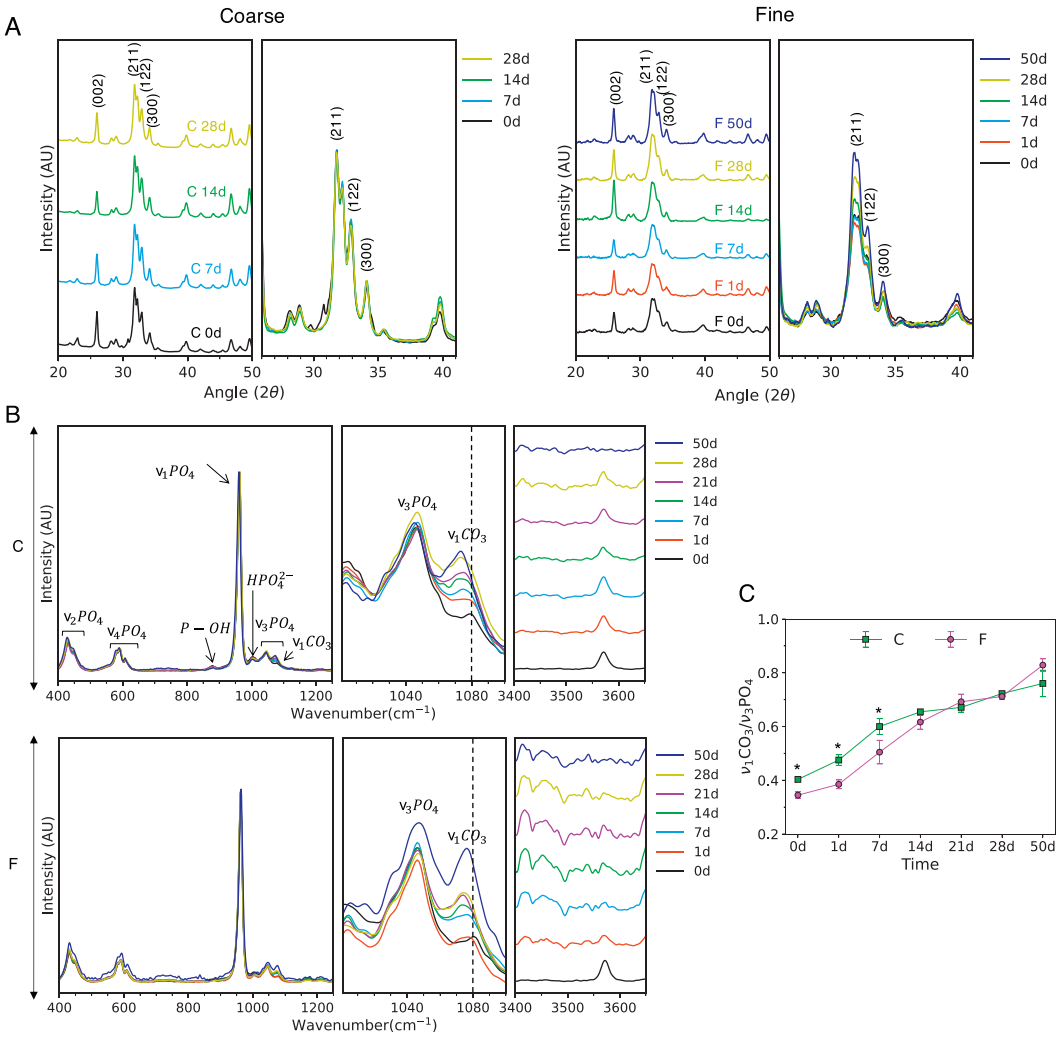

Fig. 3. (A) Grazing incidence X-ray diffraction of coarse and fine discs incubated in complete AdvDMEM. (B) Normalized Raman spectra collected from point measurements of the disc surfaces of coarse (top: marked as "C") and fine (bottom: marked as "F") discs incubated over 0 h and 1, 7, 14, 21, 28, and 50 days of incubation in complete AdvDMEM. (C) Calculated intensity ratio of $v_1CO_3^{2-}/v_3PO_4^{3-}$ bands. Bars represent means ± SD of triplicate disc measurements, and "*" indicates statistically significant differences between C and F at each time point. AdvDMEM, Advanced Dulbecco's Modified Eagle's Medium.

of 1234 different proteins identified among C7d 1, C7d 2, C7d 3, F7d 1, F7d 2, F7d 3, CM 1, and CM2), was to clearly identify clustering/correlations of proteins per sample type (C, F, and CM). Three clusters, corresponding to different sample types (C, F, or CM), were identified. This implies that consistent protein profiles were observed within replicates suggesting high repeatability of the study for each of the conditions.

The Venn diagram in Fig. 7B further shows the number of proteins identified in the C or F substrates, taking into consideration only the proteins that showed up in all replicates and not the ones appearing only in one or two replicates. One hundred fifty-two proteins were found to be in common for C and F, 71 were unique for C, and 136 were unique for F.

Table 1
Crystallite sizes of the CDHA discs incubated in culture medium.

Incubation day	Crystallite size (002) [nm]	
	Coarse	Fine
0	26.6	23.6
1	n.d.	23.7
7	27.8	24.1
14	27.2	24.4
28	28.5	25.6
50	n.d.	26.8

*n.d: not determined.

Additional analyses were made by plotting heat maps of the common proteins shared between C and F samples (Fig. 8). This representation allows to visually assess differences in terms of protein abundance per sample (red-highly abundant, blue-low abundance). The data was normalized row-wise using Z-score to visualize differences between replicates. In addition, proteins with abundances significantly different between the samples were marked with '*', and proteins particularly important in bone regeneration processes have been identified with letter 'a'. The list of these proteins with their corresponding roles, collected from literature, DAVID and STRING databases, are displayed in Table 3. Notable differences were observed between sample groups. As far as ALB*, AHSG*, GC*, F2, C3*, ACTB*, APOE, SERPINF2*, KNG1, FGA*, C7, CLU, and RIOX1 are concerned, they were more abundant for F specimens than the C ones (statistical differences marked with "*"). Proteins such as SPP2*, MGP*, ADIPOQ, C9, OSTF1, SPP1, IGF2, OMD, and MAPK13 were classified as more abundant for coarse specimens, but only a few were identified with statistically significant differences (SPP2 and MGP). Regarding BGLAP and NCDN, they showed similar abundances for both F and C hydroxyapatite discs.

3.5.2. *Gene Ontology (GO) and pathway analysis*

To gain more knowledge on the processes where the detected proteins are involved to, we used the GO bioinformatics database to classify the

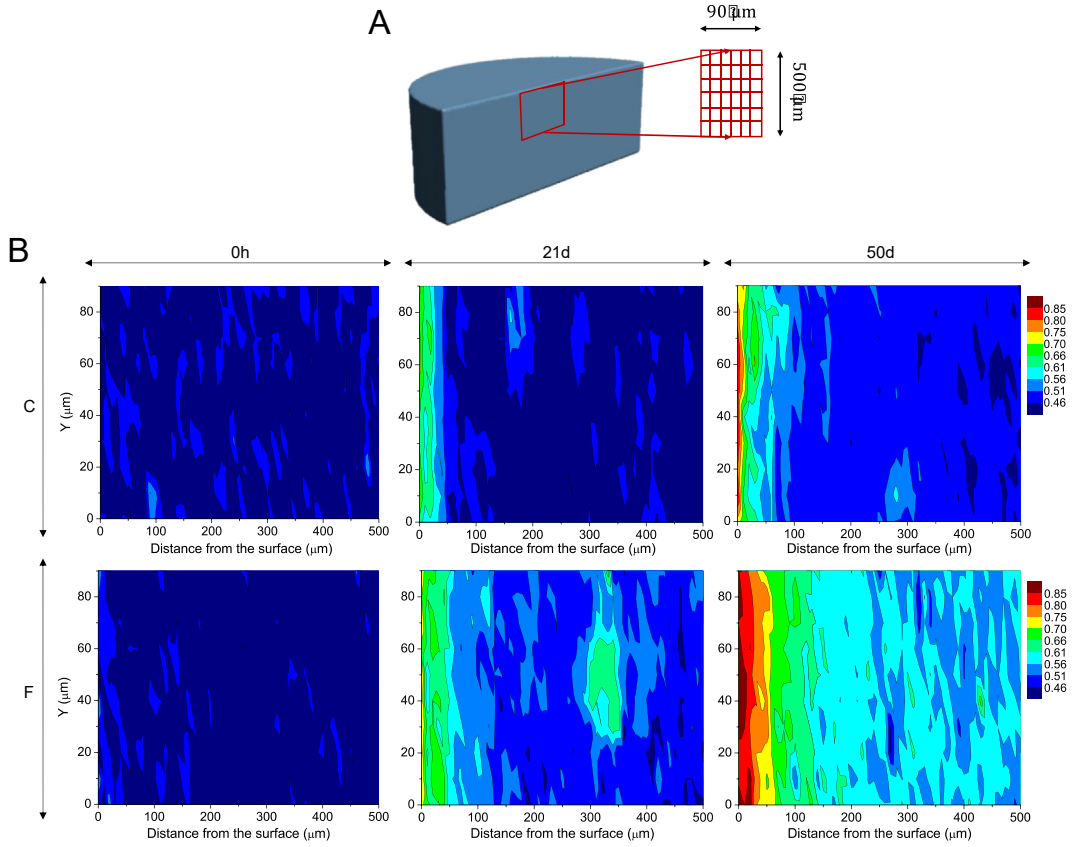

Fig. 4. (A) A schematic of the region of the samples analyzed by Raman microscopy; (B) carbonate mapping obtained by confocal Raman microscopy by representing the ratio between the intensity of $\nu_1 CO_3^{2-}/\nu_3 PO_4^{3-}$ bands of coarse (C) and fine (F) discs incubated over 0 h and 21 and 50 days in complete AdvDMEM. At the top a schematic picture showing the location of the measured region. AdvDMEM, Advanced Dulbecco's Modified Eagle's Medium.

identified proteins according to the cellular location where the protein performs its function (Cellular Component [GO CC]) and the biological process in which the protein is involved in (Biological Processes, GO BP). In addition, the Reactome pathway database was also used to classify the detected proteins participating in particular cellular pathways. Fig. 9 displays a series of graphs plotting protein abundance (emPAI) per sample and protein type involved in specific GO and Reactome pathways related to bone remodeling processes. Various points can be highlighted. First of all, it is worth mentioning that comparisons in absolute values of protein abundance are only possible between C and F samples as they have the same dimensions, and not with respect to the CM. In this respect, F substrates tend to present an overall higher abundance of proteins than C, consistent with its superior specific surface area. However, C replicates – in some specific pathways and despite its low specific surface area – do have a superior content of certain proteins than F, proving selectivity in protein adsorption as was already detected in the heatmap plot (Fig. 8). In addition, protein selectivity is also demonstrated by the enrichment of certain proteins in the samples when compared to the relative presence of that protein in the cell culture medium. Thus, we could see for instance in the GO belonging to bone resorption that C and F samples selectively adsorb more SPP1 than IAPP from the cell culture medium; or in the GO relative to regulation of bone mineralization the relative abundance of OMD and BGLAP is superior in the F and C substrates than in the culture medium, where it is not even detected.

If we look more in depth into which pathways are favored on F samples, these include the GO terms classified as GO:0005577: fibrinogen complex, which relates to clot formation; GO:0070372: regulation of ERK 1 and ERK 2 cascade, which is a central signaling pathway that regulates multiple cellular processes; GO:0006956: complement activation, which is part of the immune system; GO:0045669: positive regulation of osteoblast differentiation; and GO:0030500: regulation of bone mineralization. With regards to the Reactome pathways, F samples dominate (i.e. higher abundance of related proteins) the following cellular pathways: BTA-140877: clotting cascade; BTA-977606: regulation of complement cascade; BTA-114608: platelet degranulation; and BTA-381426: regulation of insulin-like growth factor transport and uptake by insulin-like growth factor–binding proteins (IGFBPs); all of them were involved in bone homeostasis [63,79,80]. In the case of GO:0010640: platelet-derived growth factor (PDGF) receptor signaling pathway and GO:0071634: transforming growth factor-β (TGF-β) production, similar levels for both disc types C and F were detected, excluding C7d 1 sample outlier behavior. Slightly higher protein abundance taking part in GO:0045453: bone resorption was observed for C specimens.

Moreover, some proteins which levels were not detectable or low for the culture medium were identified for CDHA discs, showing their particular affinity for the material. For instance, F7 and HSP90AB1 take part in the regulation of PDGF receptor signaling pathway (GO:0010640) and TGF-β production (GO:0071634), respectively. In addition, CLIC1 (taking part in positive regulation of osteoblast differentiation), OMD, and BGLAP (taking part in regulation of bone mineralization) proteins also showed specificity to CDHA.

3.6. *In vitro response of human mesenchymal stem cells to matured CDHA*

To prove the extent to which maturation and protein adsorption might had altered the surface properties of the materials, *in vitro* cell culture assays with human mesenchymal stem cells (hMSCs) were performed comparing pristine materials with materials incubated up to 40 days in the cell culture medium. The proliferation of hMSCs relative to substrate area at 6 h and 3 days and 14 days of cell culture on pristine (C0d and F0d) and matured CDHA discs (C40d and F40d) – incubated

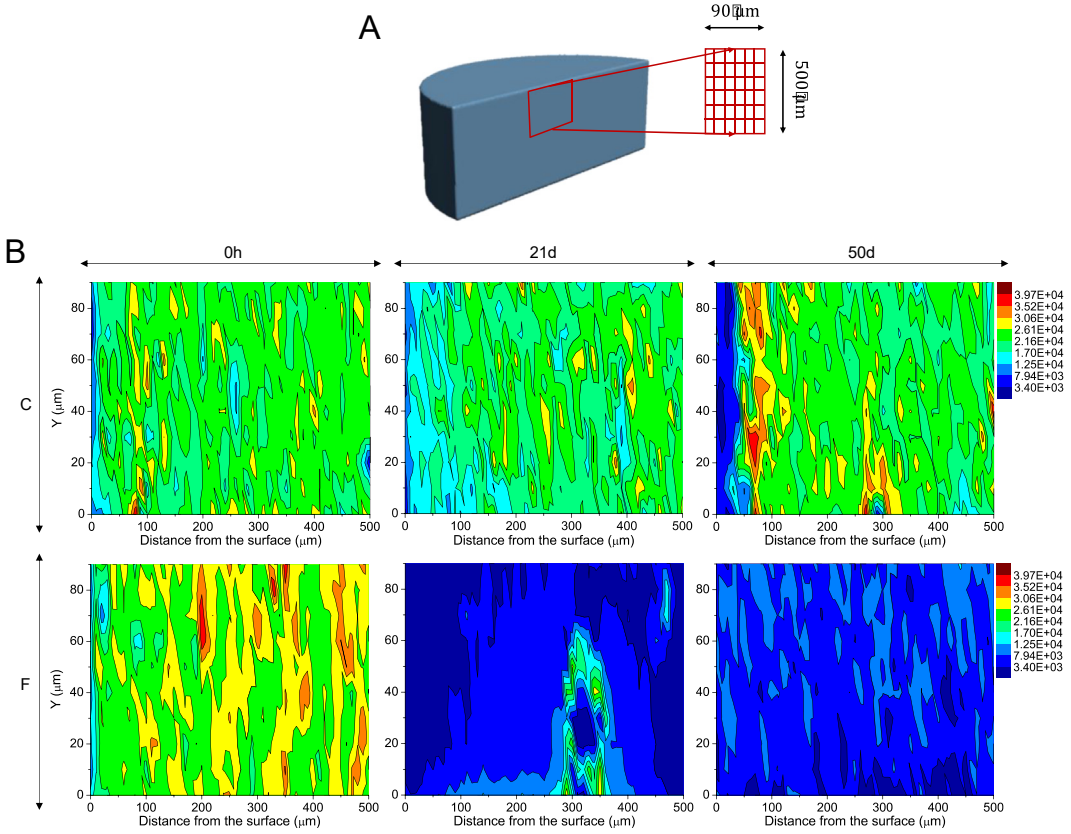

Fig. 5. (A) A schematic of the region of the samples analyzed by Raman microscopy; (B) Confocal Raman microscopy OH^- stretch intensity mapping of coarse (C) and fine (F) discs incubated over 0 h and 21 and 50 days in complete AdvDMEM. At the top, a schematic picture showing the location of the measured region. AdvDMEM, Advanced Dulbecco's Modified Eagle's Medium.

over 40 days in cell culture medium (complete AdvDMEM) – is depicted in Fig. 10A. The matured CDHA discs, both C and F, showed significantly higher cell proliferation than their non-incubated counterparts at each time point. F and C matured discs showed similar cell proliferation at 6 h and 3 days of cell culture, whereas at day 14 they exhibited significantly high cell proliferation levels when compared to TCPS control. Cell proliferation at 14 days proved to be the greatest and significantly larger for fine microstructure than coarse one of the matured CDHA.

The cell morphology was analyzed by SEM as illustrated in Fig. 10B. Similar cell morphology, exhibiting rounder not yet well-stretched shapes, and good cell adherence were observed for all the sample types at 6 h; however better spreading was noticed on F40d. Significant differences between the matured (C40d and F40d) and as-consolidated (C0d and F0d) CDHA discs could be appreciated at day 3 and 14 of cell culture where significantly higher number of cells was visible for the matured specimens; this effect was especially visible for fine microstructure. It has to be mentioned that C0d images did not represent fully the cell proliferation results, but rather showed discordance with cell number/mm^2 obtained for four replicates in Fig. 10A and should be viewed with caution. For both C40d and F40d at day 3 and for C40d at day 14, cells with well stretched spindle-like morphology could be observed. In case of F40d, a monolayer of cells was formed at day 14 which drastically contrasted with the lack of cells at the surface of the F0d, non-incubated CDHA counterpart, substrate.

4. Discussion

In contrast to the high stability of stoichiometric hydroxyapatite, non-stoichiometric nanoapatites are known to be more reactive [18,81–83]. The degree of reactivity depends on compositional features, such as the presence of vacancies or substituents in the crystalline structure, and structural features such as crystal size and crystallinity. This correlation underpins the adaptation to biological function of biological apatites in the bone and teeth and provides a powerful tool for tuning the properties of apatitic bone substitutes [84].

In this study, we analyzed the maturation in physiological fluids of two biomimetic apatites obtained from the hydrolysis of α-TCP, which results in a nanostructured CDHA with composition $Ca_9(PO_4)_5(HPO_4)(OH)$. We devoted special attention to the role of the textural properties, focusing on two sample types: F-CDHA and C-CDHA, both chemically identical but F having double the SSA than C to favor reactivity. In terms of microstructure F-CDHA consisted of an entangled network of poorly crystalline needle-like nanometric crystals and C-CDHA of larger and more crystalline plate-like crystals. Previous *in vitro* studies on these materials showed impaired cell viability, especially for the more reactive F-CDHA due to the drastic alteration of the culture medium composition due to ionic exchanges [85], whereas excellent biocompatibility was found *in vivo* for both materials, F-CDHA showing superior osteoinductive and osteogenic properties [8].

The results obtained proved substantial differences in the extent and rate of maturation between F and C samples. The ICP analysis provided the average ionic concentrations in the cell culture medium during incubation and in the solid samples themselves and were consistent and in agreement with previous works [14,24,25]. For both samples, ionic movement occurred from and to the sample. Overall, both samples absorbed Ca^{2+} and Mg^{2+} from the culture medium, whereas little variation of P_i was recorded (except for day 1 for F samples where release of P_i was observed) (Fig. 6A). Even though the ionic exchange tended to level off progressively after one day, F-CDHA still absorbed calcium even after fifty days of incubation, with daily renewal of the medium.

No changes in the microstructure of the samples were observed (Fig. 2) on the contrary to a previous report on octacalcium phosphate

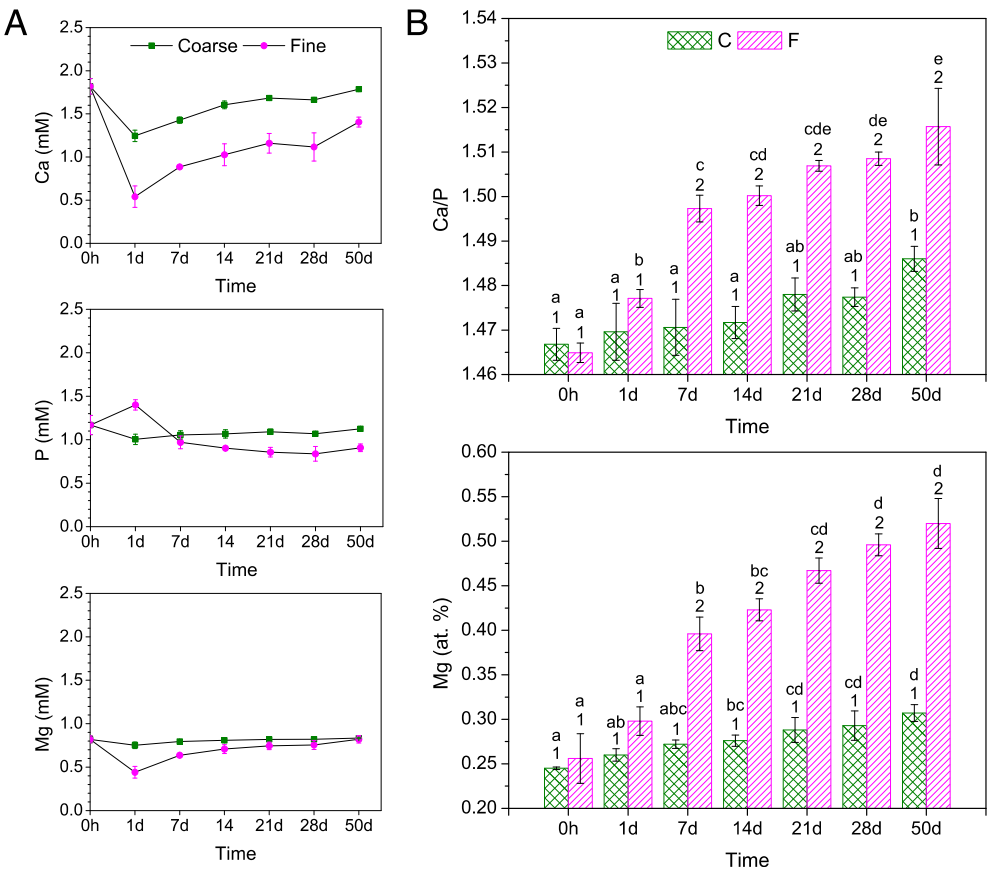

Fig. 6. (A) Concentration of Ca^{2+}, P_i and Mg^{2+} in the supernatants at 0 h, 1, 7, 14, 21, 28, and 50 days of incubation of C and F discs in complete AdvDMEM. (B) Evolution of the Ca/P molar ration and atomic Mg percentage from digested C and F discs following incubation in complete AdvDMEM for different time points: 0 h and 1, 7, 14, 21, 28, and 50 days. Groups identified by the same superscripts are not statistically different ($p>0.05$). Numbers (1 or 2) identify differences ($p<0.05$) between C and F at each time point, whereas letters (a, b, c, d, e) indicate differences ($p<0.05$) between time points within the same sample. AdvDMEM, Advanced Dulbecco's Modified Eagle's Medium.

(OCP) and low crystalline bone-like carbonated apatite (BCA) coatings [86]. The morphological changes observed in the study by Barrère et al. [86] can be explained by the superior reactivity of OCP and BCA (OCP is a transient and thermodynamically unstable phase while BCA was reported to be poorly crystalline with high carbonate content in their structure) and to the fact that the maturation study was performed in the serum-free cell culture medium that has been shown to be more reactive than when proteins are present [87]. Because there were no observable alterations in the microstructure of the samples (Fig. 2, SEM before/after incubation) and no new phase formation (XRD in Fig. 3A), these ionic exchanges should be attributed to an evolution of the pre-existing apatitic phase. The maturation of nanoapatites in solution involves both an increase in crystallinity and the evolution of the elemental composition toward stoichiometric hydroxyapatite [20,88,89]. A progressive increase in crystallinity of the fine CDHA with incubation time was corroborated using XRD, with the observation of more intense and better resolved peaks with incubation time (Fig. 3A), associated with larger crystalline domains. In contrast, lower increase in crystallinity of coarse specimens was observed because of its already intrinsic higher crystallinity.

Regarding the composition of the solid samples, a continuous increase of the Ca/P ratio was observed, significantly more pronounced and faster for the F-CDHA (Fig. 6B). The increase in the Ca/P ratio with incubation time is consistent with a previous report by Vandecandelaere et al. (2012) [82] where Ca^{2+} ions were reported to be incorporated in higher amounts than P_i during maturation of biological apatites, indicating an evolution toward stoichiometric HA. The Ca/P increase did not level off in any of the samples even after fifty days of incubation, suggesting that equilibrium was not reached in this timeframe. There was also the simultaneous incorporation of other divalent cations available in the culture medium such as Mg^{2+} (Fig. 6A and B) [21]. Moreover, Raman analysis showed that there was also an uptake of carbonate (Figs. 3C and 4), while the amount of OH decreased (Fig. 5).

The exact location of these ions in the material cannot be concluded from the results obtained in this work. It has been reported that during apatite nanocrystals growth in low-temperature/biomimetic conditions a metastable surface hydrated layer is formed surrounding the apatitic crystal [82,90,91]. This hydrated layer can contain water and labile divalent ions such as Ca^{2+}, Mg^{2+}, HPO_4^{2-}, and CO_3^{2-}, easily exchangeable with other ions from the surrounding medium [18,22,83]. It is believed that the presence of the hydrated layer is responsible for the high reactivity of biomimetic apatites [82,90,91] and that during the maturation process this layer would tend to disappear favoring the progressive growth of crystalline apatitic domains, in agreement with what has been

Table 2
Number of proteins and protein abundance based on emPAI count detected for coarse specimens (C7d 1, C7d 2, and C7d 3), fine specimens (F7d 1, F7d 2, and F7d 3), and complete AdvDMEM (CM 1 and CM 2). Values labelled with different letters (number of identified proteins) or numbers (total emPAI count) indicate statistically significant differences ($p<0.05$). ALB (albumin) was excluded from the emPAI count because of saturation due to its high abundance.

	$C^{a,1}$			$F^{a,b,2}$			$CM^{b,3}$	
	C7d 1	C7d 2	C7d 3	F7d 1	F7d 2	F7d 3	CM 1	CM 2
Number of identified proteins	469	474	502	460	465	454	433	447
Total emPAI count	274	351	375	1082	1093	1078	455	508

EmPAI, exponentially modified protein abundance index; AdvDMEM, Advanced Dulbecco's Modified Eagle's Medium.

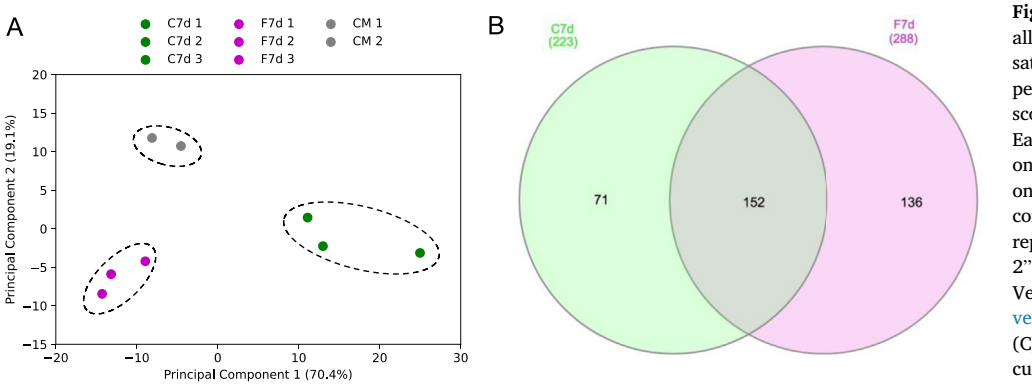

Fig. 7. (A) The PCA scatter plot derived from all 1234 detected proteins (excluding oversaturated ALB) identified by at least 2 unique peptides and their corresponding emPAI scores for all replicates of C7d, F7d and CM. Each differentially colored dot corresponds to one biological replicate. Clustering was based on protein similarity for two first principal components, where "Principal Component 1" represents 70.4% and "Principal Component 2" represents 19.1% of the total variance. (B) Venn diagram analysis (http://www.interactivenn.net/) of overlapping proteins for coarse (C) and fine (F) specimens at 7 days of incubation. The total number of proteins used to prepare the Venn diagram was filtered to the occurrence in each of the replicates. emPAI, exponentially modified protein abundance index; PCA, principal component analysis.

found in the XRD analysis and from crystallite size (002) calculated using Scherrer's formula more pronounced for fine than for coarse crystal morphology (Fig. 3A and Table 1) [90–92]. Therefore, carbonate could either be exchanged by phosphate, hydrogenophosphate, or hydroxyl ions in the crystalline structure, in the first case creating the corresponding vacancies to maintain the charge balance or incorporated in the hydrated layer. It is worth mentioning that simultaneous substitution of Ca^{2+} by Na^{+} and PO_4^{3-} by CO_3^{2-} are also possible, without any vacancy creation [84]. Overall, the unavoidable maturation of CDHA, although entailing an increase in crystallinity, does not necessarily imply

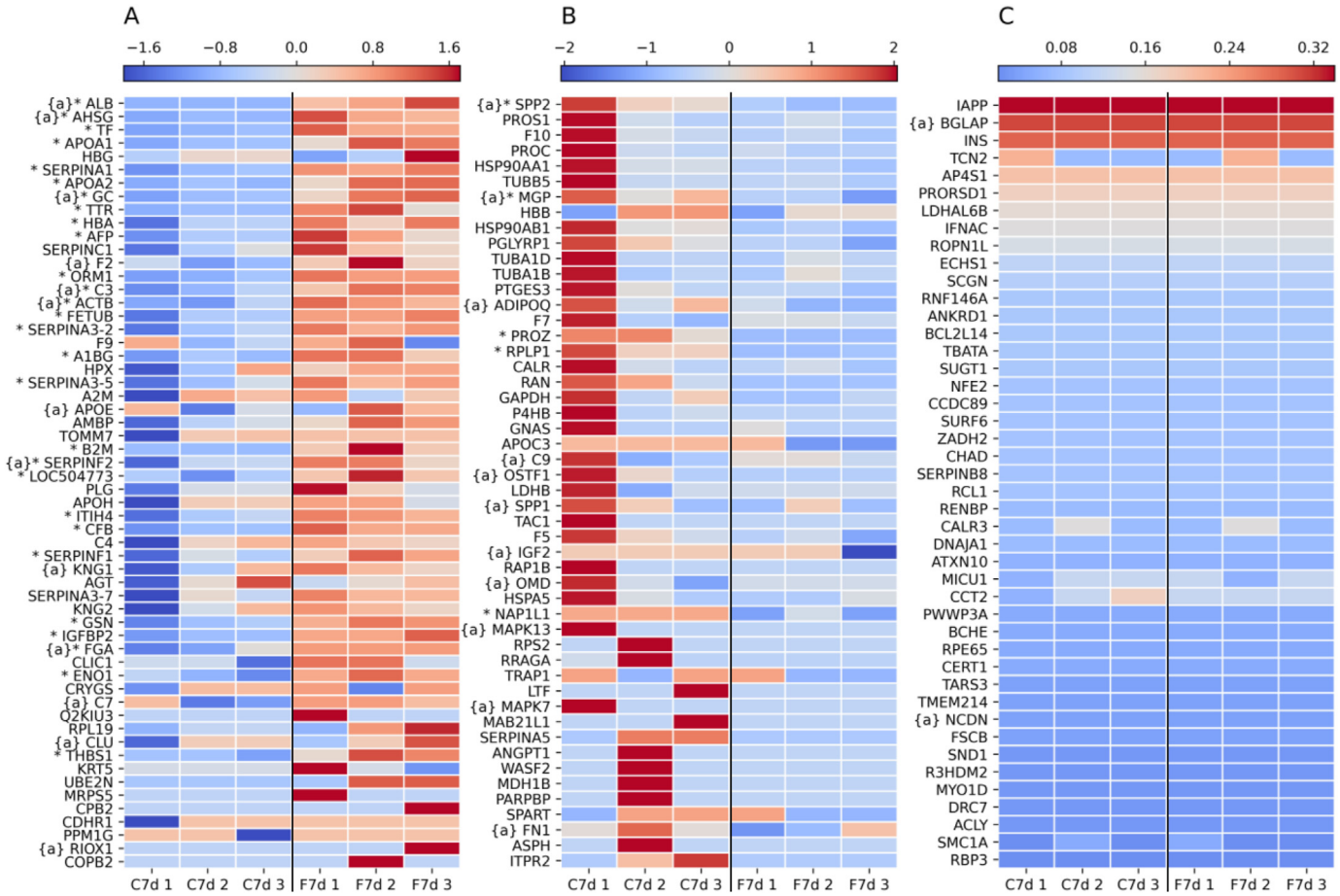

Fig. 8. Heat maps showing results of emPAI analysis for common proteins detected in each of C and F replicates. (A) Proteins detected with emPAI higher for F specimens (mean value) than for C ones (mean value) with the results Z-score normalized row-wise and sorted in the descending protein abundance order for the F sample. (B) Identified proteins with emPAI higher for C specimens (mean value) than for F ones (mean value) with the results Z-score normalized row-wise and sorted in the descending order for the values obtained for C. (C) Proteins detected at the same level of the means for C and F specimens sorted in the descending order for values obtained for C and F. Significant differences of the emPAI values for multiple testing with Benjamin-Hochberg FDR correction of each protein between groups C and F are marked with "*" (p-value <0.05). Proteins classified as important in the processes of bone regeneration are marked with "{a}". emPAI, exponentially modified protein abundance index; FDR, false discovery rate.

Table 3
Bone regeneration-related proteins adsorbed on C7d and F7d specimens where the ones in '**bold**' showed higher quantities for fine, '*cursive*' for coarse specimens, and 'regular' equal for both. Statistical differences are marked with "*". Biological functions as given by DAVID bioinformatics database (www.david.ncifcrf.gov), STRING database (https://string-db.org/), and/or literature review.

UniProtKB	Protein name	Gene name	Molecular weight (kDa)	Function
P02769	Albumin	**ALB***	69.293	Induces endogenous stem cells recruitment and promotes the growth of new bone [55–57]
P12763	Alpha-2-HS-glycoprotein	**AHSG***	38.419	Ossification and regulation of bone mineralization [58–61]
Q3MHN5	Vitamin D-binding protein	**GC***	53.342	Regulates vitamin D availability enhancing bone resorption processes [41,62]
Q2UVX4	Complement C3	**C3***	187.253	Osteoclast induction [30,40]
Q29RQ1	Complement C7	**C7**	93.09	Modulate bone regeneration and healing after fracture, allow communication
Q3MHN2	Complement C9	*C9*	61.998	of osteoblasts and osteoclasts through complement-mediated signaling [63]
P00735	Prothrombin	**F2**	70.506	Positive regulation of cell proliferation, positive regulation of cell growth, positive regulation of release of sequestered calcium ion into cytosol, regulation of cytosolic calcium ion concentration [64]
P60712	Actin, cytoplasmic 1	**ACTB***	41.737	Wnt signaling pathway [65,66]
P28800	Alpha-2-antiplasmin	**SERPINF2***	54.711	Positive regulation of cell differentiation, positive regulation of JNK cascade, positive regulation of ERK1 and ERK2 cascade, positive regulation of TGF production [67,68]
P01044	Kininogen-1	**KNG1**	68.89	Positive regulation of cytosolic calcium ion concentration, bone metabolism and regeneration [42]
Q03247	Apolipoprotein E	**APOE***	35.98	Bone metabolism and regeneration [40,42]
P02672	Fibrinogen alpha chain	**FGA***	67.012	Formation of fibrin [64,69,70]
P17697	Clusterin	**CLU**	51.114	Involved in protection against inflammatory disorders [42]
A5PK74	Ribosomal oxygenase 1	**RIOX1**	74.349	Regulates osteoblast differentiation via its interaction with SP7/OSX [71]
Q3Y5Z3	Adiponectin	*ADIPOQ*	26.133	Found to regulate mobilization and recruitment of bone marrow mesenchymal stem cells (BMSCs) in bone healing by promoting osteogenesis [72,73]
P07456	Insulin-like growth factor II	*IGF2*	19.682	Ossification [74]
Q27967	Secreted phosphoprotein 24	*SPP2**	23.134	Takes part in bone remodeling
P31096	Osteopontin	*SPP1*	30.904	Involved in ossification, osteoblast differentiation, and positive regulation of bone resorption
P07589	Fibronectin	*FN1*	272.154	Involved in osteoblast compaction in the process of fibrillogenesis essential for osteoblast mineralization, takes part in the regulation of type I collagen deposition by osteoblasts, osteoblasts are known to depend on fibronectin for differentiation and subsequently for survival [75]
Q3T0N5	Mitogen-activated protein kinase 13	*MAPK13*	42.229	Involved in chondrocytes, osteoblasts and osteoclasts differentiation through p38 MAPK pathway [76]
Q8MJ50	Osteoclast-stimulating factor 1	*OSTF1*	23.842	Induces bone resorption, osteoclast formation and activity [77]
O77742	Osteomodulin	*OMD*	49.116	Regulates bone mineralization and cell adhesion
P07507	Matrix Gla protein	*MGP**	12.217	Regulates bone mineralization through Wnt/β-catenin signaling pathway [78]
Q2KJ97	Neurochondrin	NCDN	78.799	Involved in bone resorption processes
P02820	Osteocalcin	BGLAP	11.042	Takes part in osteoblast differentiation and bone mineralization

JNK, c-Jun N-terminal protein kinase; ERK1, extracellular-signal-regulated kinase 1; ERK2, extracellular-signal-regulated kinase 2; TGF, transforming growth factor; SP7/OSX, transcription factor SP7/osterix; MAPK, mitogen activated protein kinase.

a drastic reduction of reactivity, as in addition to preserving the nanosize it also involves the incorporation of different ions such as Mg^{2+} and CO_3^{2-}, which prevent CDHA from reaching stoichiometry and are known to increase solubility.

Working with biomimetic apatites is not only challenging because of their ionic reactivity. Factors such as crystal morphology and porosity, in addition to affecting reactivity, can impact protein adsorption and, in turn, the biological behavior of the biomaterial. Moreover, the use of fetal bovine serum as protein source represents a very complex system in terms of protein number (with hundreds of different proteins), differences in protein relative abundance, aggravated by the fact that protein adsorption is a dynamic process. Precisely because protein adsorption is dynamic, we choose to run the proteomics study after 7 days of incubation – with daily medium renewal – to be able to capture the enrichment of less abundant proteins with more affinity for the material. Regarding the representation of the results, we chose to report emPAI protein abundance values per sample instead of normalizing the emPAI value per SSA. This was done because in any *in vivo* assay a given volume of material is tested, irrespective of their SSA (full record of emPAI values in the supplementary information). Moreover, because the tested materials are porous, with different pore entrance sizes, different depths of protein penetrations are to be expected, which makes impossible to know the actual surface or the material exposed to the liquid medium.

The proteomics study showed that both C and F specimens have great protein adsorption capacity, with 152 common proteins detected in all the replicates (The full list of adsorbed proteins with their emPAI abundances is available in the supplementary information). F samples, with higher SSA and larger pore entrance sizes, were capable of adsorbing three times as much protein as C samples, with special affinity for blood-related-processes proteins as given by emPAI results (Table 2). One aspect worth noticing was the selectivity of some proteins either for the C samples – despite its lower SSA – and others for F samples. This was particularly striking because chemically both materials are identical. Along the same line, if we look at the population of non-common proteins present in both substrates, we observe 71 proteins exclusively present in C samples while 136 proteins are solely present in F samples. Although one could argue that the F substrate because of their high SSA would be expected to capture more proteins, the 71 proteins detected for the C samples is a non-negligible population. This, again, puts forward differences between both biomimetic materials.

When looking more into detail the list of adsorbed proteins common on both substates we could further separate them into those essential for bone regeneration (Table 3). On the F substrate, higher levels of proteins such as ALB, AHSG*, GC*, F2, C3*, ACTB*, APOE, SERPINF2*, KNG1, FGA*, C7, CLU, and RIOX1 (Fig. 8A and Table 3) were observed, likely due to the high SSA of F. However, on C samples proteins such as SPP2*, MGP*, ADIPOQ, C9, OSTF1, SPP1, IGF2, OMD, and MAPK13 were more abundant than in F substrates. Several arguments can be put forward to explain protein selectivity between samples: differences in the crystal faces exposed on the C *versus* F crystals [93], as a consequence of the different crystal morphology; differences on the surface charge of the substrates; differences in the ionic microenvironment created between

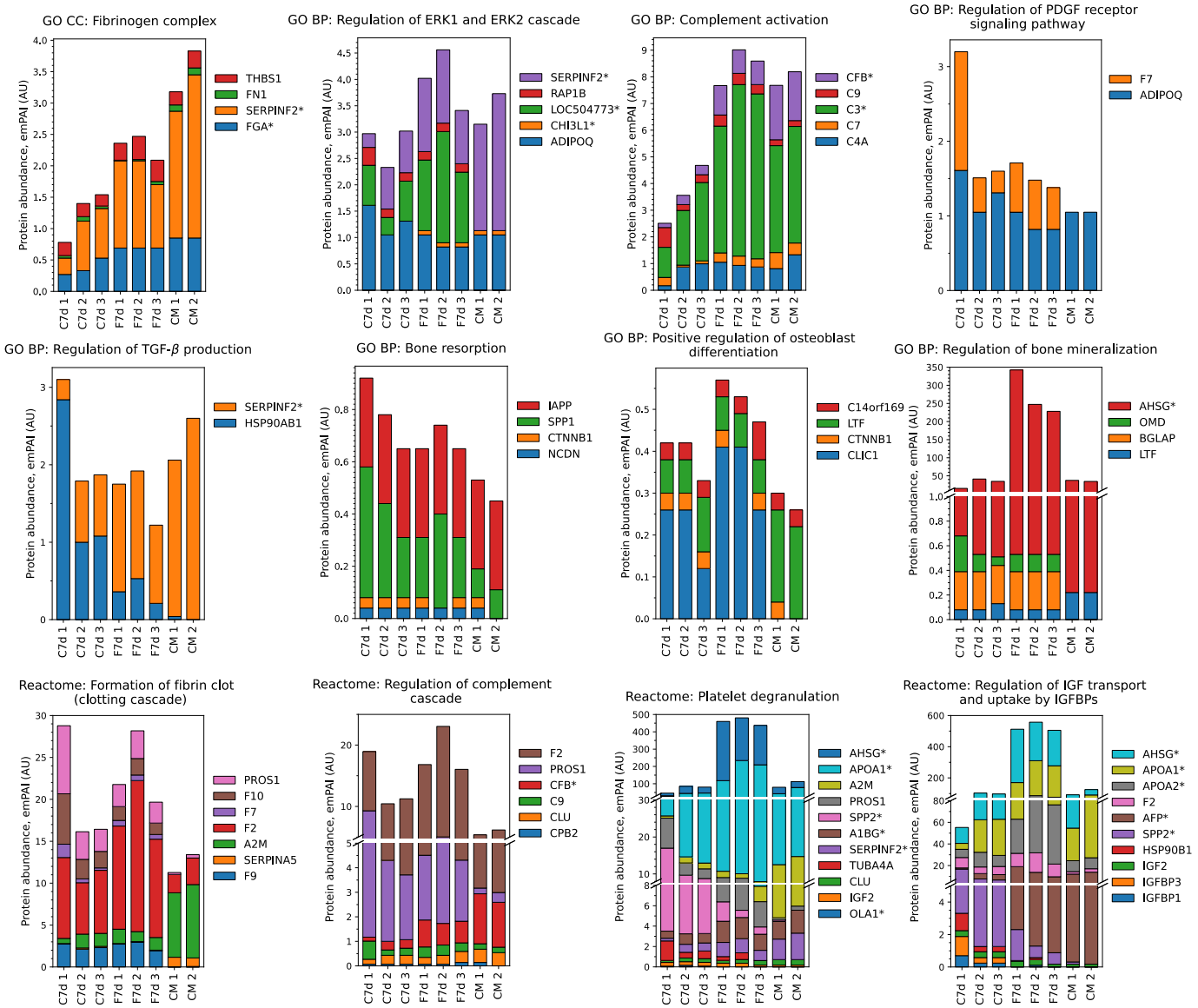

Fig. 9. Graphs showing enrichment analysis for Gene Ontology (GO) terms carried out with STRING ver. 11.0 (https://string-db.org) and further correlated with the obtained absolute emPAI results for each respective protein with no additional filtering. '*' means significant differences for multiple testing with Benjamin-Hochberg FDR correction between the average protein abundance for C and F triplicates (p-value <0.05). The GO terms and Reactome pathways have been chosen from a list of significantly enriched terms within the genes identified for all triplicates in at least one of the sample types; p-values were corrected for multiple testing using the Benjamin-Hochberg method. FDR, false discovery rate.

crystals by virtue of their different reactivities [94]; or even, protein sieving effects due to surface nanotopography [95]. It is likely that various of these mechanisms operate simultaneously. In fact, in an earlier work, we were able to prove differences in the retention ability of model proteins on F and C scaffolds by virtue of the packing density imposed by the needle-like and plate-like crystals. Because retention of proteins favors adsorption, one could expect different protein populations on both F and C, being the more close-packed substrates less prone to adsorb large proteins. In addition, because locally both C and F cause changes in the surrounding environment by the release and uptake of ions, it is likely that this leads to differences in surface charge and, in turn, in protein adsorption. In fact, we have demonstrated before that depending on the ionic environment in contact with CDHA the surface charge varies notably [94] and differences in surface and bulk liquid charge have been long associated with varied adsorption behavior of proteins [96].

Among the different types of proteins detected on the CDHA discs, some are known to take part indirectly (mediating processes of blood clotting, immune system, or complement systems) and others directly in bone regeneration (Table 3). Recruitment and differentiation of mesenchymal stem cells is orchestrated by ALB [55–57], ACTB [65,66], APOE [40], C3 [40], SERPINF2 [67,68], RIOX1 (via its interaction with SP7/OSX) [71], and ADIPOQ [72,73]. Cytosolic calcium concentration and clotting cascade resulting in formation of fibrin is modulated by KNG1 and F2 [64], as well as FGA [64,69,70]. Regulation of vitamin D by GC [41,62] indirectly enhances bone resorption processes, whereas CLU protects from acute inflammatory disorders [42]. The cross-talk between cells – osteoblasts, osteoclasts, or immune cells – is modulated by such proteins as ALB [55–57], C3, C7, and C9 [63]. Bone specific processes, such as bone resorption, osteoblast differentiation, osteoclast formation, and bone mineralization, were previously reported to be influenced by AHSG [61], IGF2 [74], FN1 [75], SPP1, SPP2, OSTF1 [77], OMD, MGP (through Wnt-β-catenin signaling pathway) [78], MAPK13 through p38 MAPK pathway [76], NCDN, and BGLAP.

Apart from the role of the abovementioned proteins in bone regeneration, GO analyses proved to be particularly interesting in assessing the role, not of individual proteins, but of groups of proteins in specific

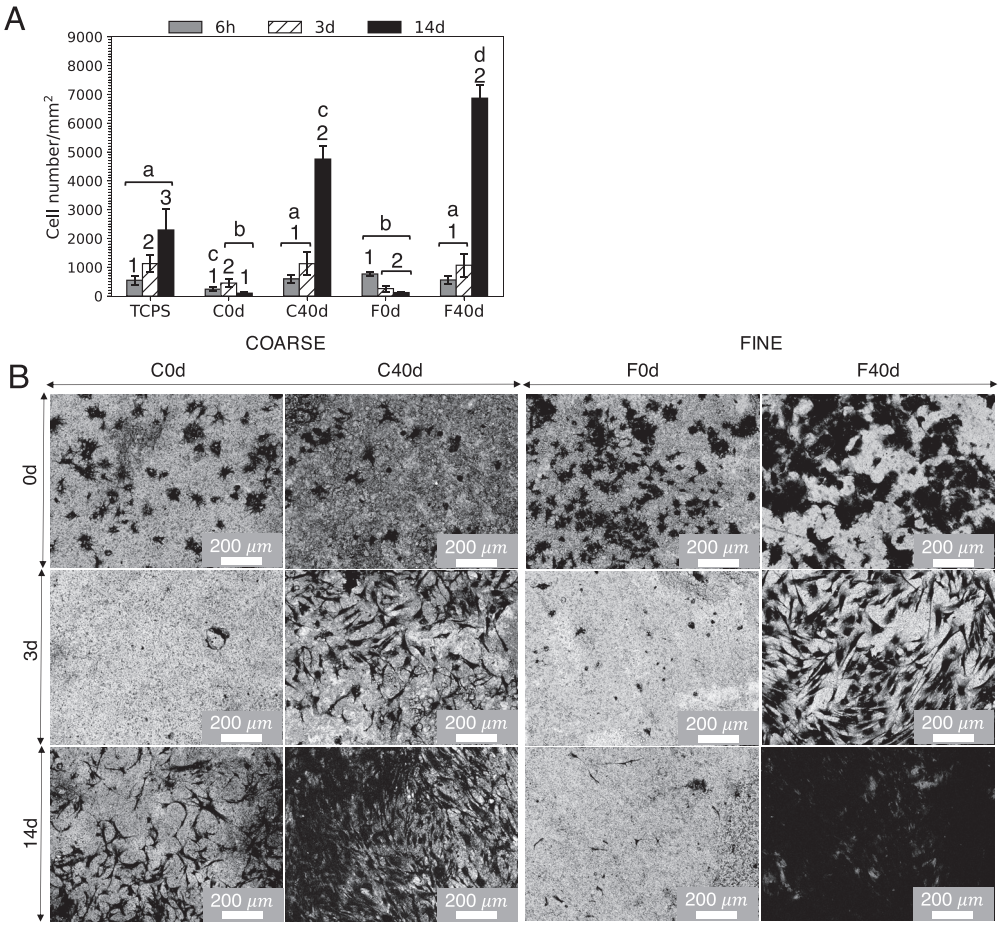

Fig. 10. (A) Proliferation of hMSCs at 6 h, 3 days, and 14 days for TCPS, C0d, C40d, F0d, and F40d. Bars represent means ± SD of four biological replicates. Different letters (a, b, c, or d) indicate significant differences ($p<0.05$) between samples for specific time points and numbers (1, 2, or 3) indicate significant differences ($p<0.05$) between time points for the given sample. (B) Morphology of hMSCs observed by SEM on C0d, C40d, F0d, and F40d over 6 h, 3 days, and 14 days of cell culture.

biological processes. The graphs in Fig. 9 compare protein abundances in the different sample groups (F, C, and CM), and this information can be used to prove the selective adsorption of proteins by CDHA, from the comparison between the relative amounts of different proteins in CM and in the F or C substrates. This highlights the special affinity of various proteins for CDHA. Most of the GO terms showed higher values of protein emPAI abundancies for F samples, i.e. a) fibrinogen complex (GO:0005577), which is considered to have pro-inflammatory and promoting effects on bone regeneration [69,97]; b) ERK 1 and ERK 2 cascade (GO:0070372) which was previously reported to positively contribute to osteogenic proliferation [67,68]; c) complement activation (GO:0006956) responsible for modulating bone regeneration and healing by allowing communication between osteoblasts and osteoclasts after bone fracture [63]; d) positive regulation of osteoblast differentiation (GO:0045669); and e) regulation of bone mineralization (GO:0030500). Bone resorption (GO:0045453) proteins were found to be more abundant for C specimens. Proteins associated to the PDGF receptor signaling pathway (GO:0010640) and TGF-β production (GO:0071634) – identified at the same level for both C and F – have an essential role in rebuilding proper vasculature in the zone of bone fracture [98,99]. In addition, proteins such as F7 (taking part in regulation of PDGF receptor signaling pathway), HSP90AB1 (taking part in TGF-β production), CLI1 (taking part in positive regulation of osteoblast differentiation), OMD, and BGLAP (taking part in regulation of bone mineralization) demonstrated particular affinity to the CDHA discs in comparison to culture medium, where they were not detected or showed very low levels. As far as the Reactome pathway terms are concerned, all of them showed higher total abundancies of identified proteins for F specimens, i.e. a) clotting cascade (BTA-140877), which results in formation of the fibrin clot that serves as a temporary structure to facilitate cellular activities and deposition of a new bone matrix [64,100]; b) regulation of the complement cascade (BTA-977606) which as mentioned before plays a key role in modulating the bone regeneration processes [63]; c) platelet degranulation (BTA-114608), which has been long known to be a source for different chemo attractants and growth factors crucial for bone remodeling such as PDGF, TGF, vascular endothelial growth factor, insulin-like growth factor (IGF) and EGF [101–103]; and c) regulation of IGF transport and uptake by IGFBPs (BTA-381426) which is an essential system for bone remodeling as both IGFBPs and IGFs were shown to, directly or indirectly (through triggering production of other factors, e.g. bone morphogenic proteins [BMPs]), stimulate proliferation and differentiation of osteoblasts and promote bone fracture healing and bone growth [104–106].

As expected, a significant enhancement in the capacity of the material to support cell proliferation was observed after maturation of the CDHA discs in the cell culture medium (Fig. 10), overcoming the *in vitro* cytotoxicity of the pristine material. Indeed, the reactive nature of pristine CDHA has a major role in the cytotoxic behavior of CDHA because of the drastic ionic changes with the cell culture medium depriving cells from e.g. Ca^{2+} [15,16]. These changes are also observed in the present study (Fig. 6A) where a drastic drop by as much as a 70% of Ca^{2+} was detected on F samples after 1 day of incubation. Importantly, incubation of the samples with medium results in sample maturation and the mitigation of these drastic changes. In fact, the results of hMSCs proliferation on CDHA

matured substrates, C and F (F > C), proved to surpass even that observed on TCPS at day 14 of culture (Fig. 10A) in contrast to previous results showing very limited cell proliferation on similar CDHA material [15,16,85]. The reason for the better performance of matured discs is reckoned to be, on one hand, the reduced effect of ion exchange as already explained [16] and, on the other hand, the favorable influence of protein adsorption on cell adhesion and proliferation [26,31]. With regards to this later aspect, the greater protein adsorption capability of the fine microstructure (F) with superior SSA than the coarse (C) one might help adsorbing and concentrating proteins relevant to proliferation contributing to the improved cell proliferation at day 14 of cell culture (Fig. 10A and B). Despite assessing cell differentiation was outside the scope of the work it is to be expected that the nature of the proteins adsorbed on the surface of the samples would play a major role during mesenchymal stem cell differentiation. These *in vitro* results put forward the limitations of static *in vitro* cell cultures as biological prescreening for estimation of *in vivo* behavior of reactive materials such as pristine CDHA. It is believed that due to its strong reactivity (C0d and F0d) the *in vivo* potential could be misinterpreted. Thus, a proper understanding and control of the material's reactivity would be needed to correctly judge the results.

Overall, the study shows that biomimetic CDHA substrates undergo a maturation process when in contact with physiological fluids. However, the extent of these reactions varies depending on structural features such as microstructure, crystallinity, or specific surface area, which modulate the inherent reactivity of the samples (F > C). Interestingly, these parameters modulate also the surface proteomic signature on F and C substrates, not only in terms of protein abundance but also in the type of proteins adsorbed. The results obtained highlight, on one hand, the existence of protein selectivity toward F or C microstructures and, on another hand, the capability of CDHA, and more remarkably of F-CDHA, to concentrate specific proteins from the culture medium. The different degrees of interaction with physiological fluids of F- and C-CDHA at the ionic and protein level proved to have an important impact on the *in vitro* behavior of these substrates where F-CDHA showed to be superior in terms of cell proliferation. As follows, the mentioned effects must certainly have consequences in the subsequent biological events that condition the *in vivo* performance and may explain the superior behavior of F-CDHA observed in previous studies by Barba et al. (2019) [8].

5. Conclusions

The results obtained in this work demonstrate the extent of the maturation process that CDHA undergoes under the exposure to biological fluids. It has been shown that the degree of reactivity of biomimetic hydroxyapatite in the cell culture medium is strongly modulated by the textural properties of the material. Needle-like morphology of larger SSA showed higher level of B-type carbonation, global Mg uptake, and Ca/P ratio increment. In contrast, the reactivity of plate-like CDHA discs of lower SSA seemed to be limited in time and localization where the evolution of the material happens on its surface with barely any penetration. The results put forward that the changes occurred in the crystal lattice or in the hydrated layer, as no proof was found of any precipitates of new phases. Protein adsorption abundance and selectivity was revealed to be dependent on such factors as microstructure, crystallinity, and SSA of CDHA substrates. Better *in vitro* performance of matured CDHA substrates indicated the important inhibiting influence of ion exchange on the *in vitro* cell culture and essentiality of protein adsorption on cell adhesion and proliferation. Hence, proteomics analysis in this study showed its potential to serve as a complementary method to *in vitro* testing for prescreening its biological potential before *in vivo* studies.

Data availability statement

The raw/processed data required to reproduce these findings cannot be shared at this time because of technical or time limitations.

Credit author statement

Joanna Konka: Methodology, Software, Validation, Formal Analysis, Investigation, Visualization, Writing - Original Draft. **Montserrat Espanol**: Conceptualization, Investigation, Writing - Review & Editing. **Begona M. Bosch**: Investigation, Visualization, Writing - Review. **Eliandre de Oliveira**: Investigation, Writing - Review. **Maria-Pau Ginebra**: Conceptualization, Supervision, Resources, Writing - Reviewing & Editing, Funding acquisition.

Declaration of competing interest

The authors declare the following financial interests/personal relationships which may be considered as potential competing interests:

MPG has an equity interest in Mimetis Biomaterials, S.L., a spin-off company of UPC that may potentially benefit from the research results displayed in the present work.

JK, ME, BMB, and EdO have no competing financial interests or personal relationships that could have appeared to influence the work reported in this paper.

Acknowledgments

This research was supported by the Spanish Ministry of Science, Innovation and Universities through the PID2019-103892RB-I00/AEI/10.13039/501100011033 project. The authors also thank the Generalitat de Catalunya for funding through projects 2017SGR-1165 and BASE3D 001-P-001646 (co-funded by the European Regional Development Fund), as well as the ICREA Academia award of MPG, the FI-AGAUR scholarship of JK, and the Serra Hunter Program of ME.

Appendix A. Supplementary data

Supplementary data to this article can be found online at https://doi.org/10.1016/j.mtbio.2021.100137.

References

[1] A. Diez-Escudero, M. Espanol, M.P. Ginebra, Chapter 5 – synthetic bone graft substitutes: calcium-based biomaterials, in: H. Alghamdi, J. Jansen (Eds.), Dental Implants and Bone Grafts: Materials and Biological Issues, Woodhead Publishing, Elsevier, 2020, pp. 127–146, https://doi.org/10.1016/C2016-0-03454-X.

[2] L.C. Gerhardt, A. Boccaccini, Bioactive glass and glass-ceramic scaffolds for bone tissue engineering, Materials 3 (7) (2010) 3867–3910, https://doi.org/10.3390/ma3073867.

[3] M.P. Ginebra, M. Espanol, Y. Maazouz, V. Bergez, D. Pastorino, Bioceramics and bone healing, EFORT Open Rev. 3 (2018) 173–183, https://doi.org/10.1302/2058-5241.3.170056.

[4] W. Habraken, P. Habibovic, M. Epple, M. Bohner, Calcium phosphates in biomedical applications: materials for the future? Mater. Today 19 (2016) 69–87, https://doi.org/10.1016/j.mattod.2015.10.008.

[5] C. Rey, C. Combes, C. Drouet, D. Grossin, G. Bertrand, J. Soulié, Bioactive calcium phosphate compounds: physical chemistry, in: P. Ducheyne, D.W. Grainger, K.E. Healy, D.W. Hutmacher, C.J. Kirkpatrick (Eds.), Comprehensive Biomaterials II, vol. 1, Elsevier, 2017, pp. 244–290, https://doi.org/10.1016/B978-0-12-803581-8.10171-7.

[6] A. Barba, A. Diez-Escudero, Y. Maazouz, K. Rappe, M. Espanol, E.B. Montufar, M. Bonany, J. Sadowska, J. Guillem-Marti, C. Öhman Mägi, C. Persson, M.C. Manzanares, J. Franch, M.-P. Ginebra, Osteoinduction by foamed and 3D-printed calcium phosphate scaffolds: effect of nanostructure and pore architecture, ACS Appl. Mater. Interfaces 9 (48) (2017) 41722–41736, https://doi.org/10.1021/acsami.7b14175.

[7] A. Barba, Y. Maazouz, A. Diez-Escudero, K. Rappe, M. Espanol, E.B. Montufar, C. Öhman Mägi, C. Persson, P. Fontecha, M.C. Manzanares, J. Franch, M.-P. Ginebra, Osteogenesis by foamed and 3D-printed nanostructured calcium phosphate scaffolds: effect of pore architecture, Acta Biomater. 79 (2018) 135–147, https://doi.org/10.1016/j.actbio.2018.09.003.

[8] A. Barba, A. Diez-Escudero, M. Espanol, M. Bonany, J.M. Sadowska, J. Guillem-Marti, C. Öhman Mägi, C. Persson, M.C. Manzanares Céspedes, J. Franch, M.-P. Ginebra, The impact of biomimicry in the design of osteoinductive bone substitutes: nanoscale matters, ACS Appl. Mater. Interfaces 11 (2019) 8818–8830, https://doi.org/10.1021/acsami.8b20749.

[9] J.M. Sadowska, F. Wei, J. Guo, J. Guillem-Marti, M.-P. Ginebra, Y. Xiao, Effect of nano-structural properties of biomimetic hydroxyapatite on

osteoimmunomodulation, Biomaterials 181 (2018) 318–332, https://doi.org/10.1016/j.biomaterials.2018.07.058.
[10] P. Habibovic, J. Barralet, Bioinorganics and biomaterials: bone repair, Acta Biomater. 7 (8) (2011) 3013–3026, https://doi.org/10.1016/j.actbio.2011.03.027.
[11] A.M.C. Barradas, H. Yuan, C.A. van Blitterswijk, P. Habibovic, Osteoinductive biomaterials: current knowledge of properties, experimental models and biological mechanisms, Eur. Cell. Mater. 21 (2011) 407–429, https://doi.org/10.22203/ecm.v021a31.
[12] V.P. Galvan-Chacon, P. Habibovic, Deconvoluting the bioactivity of calcium phosphate-based bone graft substitutes: strategies to understand the role of individual material properties, Adv. Healthc. Mater. 6 (13) (2017) 1601478, https://doi.org/10.1002/adhm.201601478.
[13] E. Engel, S.D. Valle, C. Aparicio, G. Altankov, L. Asin, J.A. Planell, M.-P. Ginebra, Discerning the role of topography and ion exchange in cell response of bioactive tissue engineering scaffolds, Tissue Eng. A 14 (8) (2008) 1341–1351, https://doi.org/10.1089/ten.tea.2007.0287.
[14] K. Klimek, A. Belcarz, R. Pazik, P. Sobierajska, T. Han, R.J. Wiglusz, G. Ginalska, "False" cytotoxicity of ions-adsorbing hydroxyapatite - corrected method of cytotoxicity evaluation for ceramics of high specific surface area, Mater. Sci. Eng. C 65 (2016) 70–79, https://doi.org/10.1016/j.msec.2016.03.105.
[15] J.M. Sadowska, J. Guillem-Marti, E.B. Montufar, M. Espanol, M.-P. Ginebra, Biomimetic versus sintered calcium phosphates: the in vitro behavior of osteoblasts and mesenchymal stem cells, Tissue Eng. A 23 (23–24) (2017) 1297–1309, https://doi.org/10.1089/ten.tea.2016.0406.
[16] J.M. Sadowska, J. Guillem-Marti, M. Espanol, C. Stähli, N. Döbelin, M.-P. Ginebra, In vitro response of mesenchymal stem cells to biomimetic hydroxyapatite substrates: a new strategy to assess the effect of ion exchange, Acta Biomater. 76 (2018) 319–332, https://doi.org/10.1016/j.actbio.2018.06.025.
[17] A.R. Atif, M. Pujari-Palmer, M. Tenje, G. Mestres, A microfluidics-based method for culturing osteoblasts on biomimetic hydroxyapatite, Acta Biomater. 127 (2021) 327–337, https://doi.org/10.1016/j.actbio.2021.03.046.
[18] C. Rey, C. Combes, C. Drouet, H. Sfihi, A. Barroug, Physico-chemical properties of nanocrystalline apatites: implications for biominerals and biomaterials, Mater. Sci. Eng. C 27 (2) (2007) 198–205, https://doi.org/10.1016/j.msec.2006.05.015.
[19] C. Rey, C. Combes, C. Drouet, A. Lebugle, H. Sfihi, A. Barroug, Nanocrystalline apatites in biological systems: characterisation, structure and properties, Materialwiss. Werk- stofftech. 38 (12) (2007) 996–1002, https://doi.org/10.1002/mawe.200700229.
[20] D. Farlay, G. Panczer, C. Rey, P.D. Delmas, G. Boivin, Mineral maturity and crystallinity index are distinct characteristics of bone mineral, J. Bone Miner. Metabol. 28 (4) (2010) 433–445, https://doi.org/10.1007/s00774-009-0146-7.
[21] C. Rey, C. Combes, C. Drouet, S. Cazalbou, D. Grossin, F. Brouillet, S. Sarda, Surface properties of biomimetic nanocrystalline apatites; applications in biomaterials, Prog. Cryst. Growth Char. Mater. 60 (3) (2014) 63–73, https://doi.org/10.1016/j.pcrysgrow.2014.09.005.
[22] C. Drouet, M. Aufray, S. Rollin, N. Vandecandelaere, D. Grossin, F. Rossignol, E. Champion, A. Navrotsky, C. Rey, Nanocrystalline apatites: the fundamental role of water, Am. Mineral. 103 (2018) 550–564, https://doi.org/10.2138/am-2018-6415.
[23] J. Gustavsson, M.-P. Ginebra, E. Engel, J. Planell, Ion reactivity of calcium-deficient hydroxyapatite in standard cell culture media, Acta Biomater. 7 (12) (2011) 4242–4252, https://doi.org/10.1016/j.actbio.2011.07.016.
[24] J. Gustavsson, M.-P. Ginebra, J. Planell, E. Engel, Osteoblast-like cellular response to dynamic changes in the ionic extracellular environment produced by calcium-deficient hydroxyapatite, J. Mater. Sci. Mater. Med. 23 (2012) 2509–2520, https://doi.org/10.1007/s10856-012-4705-4.
[25] B. Kasemo, Biological surface science, Surf. Sci. 500 (1) (2002) 656–677, https://doi.org/10.1016/S0039-6028(01)01809-X.
[26] M. Toledano, Álvaro Carrasco-Carmona, A.L. Medina-Castillo, M. Toledano-Osorio, R. Osorio, Protein adsorption and bioactivity of functionalized electrospun membranes for bone regeneration, J. Dent. 102 (2020) 103473, https://doi.org/10.1016/j.jdent.2020.103473.
[27] K. Sugimoto, S. Tsuchiya, M. Omori, R. Matsuda, M. Fujio, K. Kuroda, M. Okido, H. Hibi, Proteomic analysis of bone proteins adsorbed onto the surface of titanium dioxide, Biochem. Biophys. Rep. 7 (2016) 316–322, https://doi.org/10.1016/j.bbrep.2016.07.007.
[28] S.Y. Jung, S.M. Lim, F. Albertorio, G. Kim, M.C. Gurau, R.D. Yang, M.A. Holden, P.S. Cremer, The Vroman effect: a molecular level description of fibrinogen displacement, J. Am. Chem. Soc. 125 (42) (2003) 12782–12786, https://doi.org/10.1021/ja037263o.
[29] H. Noh, E.A. Vogler, Volumetric interpretation of protein adsorption: competition from mixtures and the Vroman effect, Biomaterials 28 (3) (2007) 405–422, https://doi.org/10.1016/j.biomaterials.2006.09.006.
[30] Z. Othman, B.C. Pastor, S. van Rijt, P. Habibovic, Understanding interactions between biomaterials and biological systems using proteomics, Biomaterials 167 (2018) 191–204, https://doi.org/10.1016/j.biomaterials.2018.03.020.
[31] S. Samavedi, A.R. Whittington, A.S. Goldstein, Calcium phosphate ceramics in bone tissue engineering: a review of properties and their influence on cell behavior, Acta Biomater. 9 (9) (2013) 8037–8045, https://doi.org/10.1016/j.actbio.2013.06.014.
[32] M.B. Gorbet, M.V. Sefton, Biomaterial-associated thrombosis: roles of coagulation factors, complement, platelets and leukocytes, Biomaterials 25 (26) (2004) 5681–5703, https://doi.org/10.1016/j.biomaterials.2004.01.023.
[33] S.H. Mollmann, U. Elofsson, J.T. Bukrinsky, S. Frokjaer, Displacement of adsorbed insulin by Tween 80 monitored using total internal reflection fluorescence and ellipsometry, Pharm. Res. 22 (2005) 1931–1941, https://doi.org/10.1007/s11095-005-7249-1.
[34] B. Douzi, Protein-Protein Interactions: Surface Plasmon Resonance, vol. 1615, Humana Press, New York, 2017, https://doi.org/10.1007/978-1-4939-7033-9_21.
[35] S.S. Vaidya, R.Y. Ofoli, Adsorption and interaction of fibronectin and human serum albumin at the liquid-liquid interface, Langmuir 21 (13) (2005) 5852–5858, https://doi.org/10.1021/la046766k.
[36] K.K. Chittur, FTIR/ATR for protein adsorption to biomaterial surfaces, Biomaterials 19 (4) (1998) 357–369, https://doi.org/10.1016/S0142-9612(97)00223-8.
[37] M.P. Schmidt, C.E. Martínez, Kinetic and conformational insights of protein adsorption onto montmorillonite revealed using in situ ATR-FTIR/2D-COS, Langmuir 32 (31) (2016) 7719–7729, https://doi.org/10.1021/acs.langmuir.6b00786.
[38] Z. Zhang, S. Wu, D.L. Stenoien, L. Paša-Tolić, High-throughput proteomics, Annu. Rev. Anal. Chem. (Palo Alto Calif) 7 (1) (2014) 427–454, https://doi.org/10.1146/annurev-anchem-071213-020216.
[39] J. Kim, Systematic approach to characterize the dynamics of protein adsorption on the surface of biomaterials using proteomics, Colloids Surf., B 188 (2020) 110756, https://doi.org/10.1016/j.colsurfb.2019.110756.
[40] H. Kaneko, J. Kamiie, H. Kawakami, T. Anada, Y. Honda, N. Shiraishi, S. Kamakura, T. Terasaki, H. Shimauchi, O. Suzuki, Proteome analysis of rat serum proteins adsorbed onto synthetic octacalcium phosphate crystals, Anal. Biochem. 418 (2) (2011) 276–285, https://doi.org/10.1016/j.ab.2011.07.022.
[41] Z. Othman, R.J.C. Mohren, B. Cillero-Pastor, Z. Shen, Y.S.N.W. Lacroix, A.P.M. Guttenplan, Z. Tahmasebi Birgani, L. Eijssen, T.M. Luider, S. van Rijt, P. Habibovic, Comparative proteomic analysis of human mesenchymal stromal cell behavior on calcium phosphate ceramics with different osteoinductive potential, Mater. Today Bio 7 (2020) 100066, https://doi.org/10.1016/j.mtbio.2020.100066.
[42] F. Romero-Gavilan, A.M. Sánchez-Pérez, N. Araújo-Gomes, M. Azkargorta, I. Iloro, F. Elortza, M. Gurruchaga, I. Goñi, J. Suay, Proteomic analysis of silica hybrid sol-gel coatings: a potential tool for predicting the biocompatibility of implants in vivo, Biofouling 33 (8) (2017) 676–689, https://doi.org/10.1080/08927014.2017.1356289.
[43] M.-P. Ginebra, E. Fernández, E.A.P.D. Maeyer, R.M.H. Verbeeck, M.G. Boltong, J. Ginebra, F.C.M. Driessens, J.A. Planell, Setting reaction and hardening of an apatitic calcium phosphate cement, J. Dent. Res. 76 (4) (1997) 905–912, https://doi.org/10.1177/00220345970760041201.
[44] M. Espanol, R. Perez, E. Montufar, C. Marichal, A. Sacco, M.-P. Ginebra, Intrinsic porosity of calcium phosphate cements and its significance for drug delivery and tissue engineering applications, Acta Biomater. 5 (7) (2009) 2752–2762, https://doi.org/10.1016/j.actbio.2009.03.011.
[45] K. Cheng, A. Sloan, S. McCorrister, L. Peterson, H. Chui, M. Drebot, C. Nadon, J.D. Knox, G. Wang, Quality evaluation of LC-MS/MS-based E. coli H antigen typing (MS-H) through label-free quantitative data analysis in a clinical sample setup, Proteom. Clin. Appl. 8 (11–12) (2014) 963–970, https://doi.org/10.1002/prca.201400019.
[46] S. McIlwain, M. Mathews, M.S. Bereman, E.W. Rubel, M.J. MacCoss, W.S. Noble, Estimating relative abundances of proteins from shotgun proteomics data, BMC Bioinf. 13 (2012) 308, https://doi.org/10.1186/1471-2105-13-308.
[47] R.H. Rice, D.M. Rocke, H.S. Tsai, K.A. Silva, Y.J. Lee, J.P. Sundberg, Distinguishing mouse strains by proteomic analysis of pelage hair, J. Invest. Dermatol. 129 (9) (2009) 2120–2125, https://doi.org/10.1038/jid.2009.52.
[48] J.C. Elliott, Chapter 4 - mineral, synthetic and biological carbonate apatites, in: Structure and Chemistry of the Apatites and Other Calcium Orthophosphates, Vol. 18 of Studies in Inorganic Chemistry, Elsevier, 1994, pp. 191–304, https://doi.org/10.1016/B978-0-444-81582-8.50009-2.
[49] A. Antonakos, E. Liarokapis, T. Leventouri, Micro-Raman and FTIR studies of synthetic and natural apatites, Biomaterials 28 (19) (2007) 3043–3054, https://doi.org/10.1016/j.biomaterials.2007.02.028.
[50] G. Penel, G. Leroy, C.C. Rey, E. Bres, MicroRaman spectral study of the PO_4 and CO_3 vibrational modes in synthetic and biological apatites, Calcif. Tissue Int. 63 (1998) 475–481, https://doi.org/10.1007/s002239900561.
[51] G. Penel, C. Delfosse, M. Descamps, G. Leroy, Composition of bone and apatitic biomaterials as revealed by intravital Raman microspectroscopy, Bone 36 (5) (2005) 893–901, https://doi.org/10.1016/j.bone.2005.02.012.
[52] J.C. Elliott, Chapter 3 - hydroxyapatite and nonstoichiometric apatites, in: Structure and Chemistry of the Apatites and Other Calcium Orthophosphates, Vol. 18 of Studies in Inorganic Chemistry, Elsevier, 1994, pp. 111–189, https://doi.org/10.1016/B978-0-444-81582-8.50009-2.
[53] A. Awonusi, M. Morris, M. Tecklenburg, Carbonate assignment and calibration in the Raman spectrum of apatite, Calcif. Tissue Int. 81 (2007) 46–52, https://doi.org/10.1007/s00223-007-9034-0.
[54] Y. Ishihama, Y. Oda, T. Tabata, T. Sato, T. Nagasu, J. Rappsilber, M. Mann, Exponentially modified protein abundance index (emPAI) for estimation of absolute protein amount in proteomics by the number of sequenced peptides per protein*s, Mol. Cell. Proteomics 4 (9) (2005) 1265–1272, https://doi.org/10.1074/mcp.M500061-MCP200.
[55] G. Skaliczki, K. Schandl, M. Weszl, T. Major, M. Kovács, J. Skaliczki, M. Szendrői, C. Dobó-Nagy, Z. Lacza, Serum albumin enhances bone healing in a nonunion femoral defect model in rats: a computer tomography micromorphometry study, Int. Orthop. 37 (4) (2013) 741–745, https://doi.org/10.1007/s00264-012-1770-8.
[56] D.B. Horváthy, G. Vácz, T. Szabó, I.C. Szigyártó, I. Toró, B. Vámos, I. Hornyák, K. Renner, T. Klára, B.T. Szabó, C. Dobó-Nagy, A. Doros, Z. Lacza, Serum albumin

coating of demineralized bone matrix results in stronger new bone formation, J. Biomed. Mater. Res. B Appl. Biomater. 104 (1) (2016) 126–132, https://doi.org/10.1002/jbm.b.33359.
[57] D.B. Horváthy, M. Simon, C.M. Schwarz, M. Masteling, G. Vácz, I. Hornyák, Z. Lacza, Serum albumin as a local therapeutic agent in cell therapy and tissue engineering, Biofactors 43 (3) (2017) 315–330, https://doi.org/10.1002/biof.1337.
[58] M. Szweras, D. Liu, E.A. Partridge, J. Pawling, B. Sukhu, C. Clokie, W. Jahnen-Dechent, H.C. Tenenbaum, C.J. Swallow, M.D. Grynpas, J.W. Dennis, α2-HS glycoprotein/fetuin, a transforming growth factor-β/bone morphogenetic protein antagonist, regulates postnatal bone growth and remodeling, J. Biol. Chem. 277 (22) (2002) 19991–19997, https://doi.org/10.1074/jbc.M112234200.
[59] J.T. Triffitt, U. Gebauer, B.A. Ashton, M.E. Owen, Origin of plasma α_2HS-glycoprotein and its accumulation in bone, Nature 262 (5565) (1976) 226–227, https://doi.org/10.1038/262226a0.
[60] S. Lissenberg-Thunnissen, D. de Gorter, C. Sier, I. Schipper, Use and efficacy of bone morphogenetic proteins in fracture healing, Int. Orthop. 35 (2011) 1271–1280, https://doi.org/10.1007/s00264-011-1301-z.
[61] B. Rittenberg, E. Partridge, G. Baker, C. Clokie, R. Zohar, J.W. Dennis, H.C. Tenenbaum, Regulation of BMP-induced ectopic bone formation by AHSG, J. Orthop. Res. 23 (3) (2005) 653–662, https://doi.org/10.1016/j.orthres.2004.11.010.
[62] J.R. Delanghe, R. Speeckaert, M.M. Speeckaert, Behind the scenes of vitamin D binding protein: more than vitamin D binding, Best Pract. Res. Clin. Endocrinol. Metabol. 29 (5) (2015) 773–786, https://doi.org/10.1016/j.beem.2015.06.006.
[63] Y. Mödinger, B. Löffler, M. Huber-Lang, A. Ignatius, Complement involvement in bone homeostasis and bone disorders, Semin. Immunol. 37 (2018) 53–65, https://doi.org/10.1016/j.smim.2018.01.001.
[64] A. Noori, S.J. Ashrafi, R. Vaez Ghaemi, A. Hatamian-Zaremi, T. Webster, A review of fibrin and fibrin composites for bone tissue engineering, Int. J. Nanomed. 12 (2017) 4937–4961, https://doi.org/10.2147/IJN.S124671.
[65] K.S. Houschyar, C. Tapking, M.R. Borrelli, D. Popp, D. Duscher, Z.N. Maan, M.P. Chelliah, J. Li, K. Harati, C. Wallner, S. Rein, D. Pförringer, G. Reumuth, G. Grieb, S. Mouraret, M. Dadras, J.M. Wagner, J.Y. Cha, F. Siemers, M. Lehnhardt, B. Behr, Wnt pathway in bone repair and regeneration – what do we know so far, Front. Cell Dev. Biol. 6 (2019) 170, https://doi.org/10.3389/fcell.2018.00170.
[66] P. Marie, E. Haÿ, Cadherins and Wnt signalling: a functional link controlling bone formation, BoneKEy Rep. 2 (2013) 330, https://doi.org/10.1038/bonekey.2013.64.
[67] F. Kantawong, K.E. Burgess, K. Jayawardena, A. Hart, R.J. Burchmore, N. Gadegaard, R.O.C. Oreffo, M.J. Dalby, Whole proteome analysis of osteoprogenitor differentiation induced by disordered nanotopography and mediated by ERK signalling, Biomaterials 30 (27) (2009) 4723–4731, https://doi.org/10.1016/j.biomaterials.2009.05.040.
[68] Z. Zhang, J. Wang, X. Lü, An integrated study of natural hydroxyapatite-induced osteogenic differentiation of mesenchymal stem cells using transcriptomics, proteomics and microRNA analyses, Biomed. Mater. 9 (4) (2014), 045005, https://doi.org/10.1088/1748-6041/9/4/045005.
[69] S.G. Santos, M. Lamghari, C.R. Almeida, M.I. Oliveira, N. Neves, A.C. Ribeiro, J.N. Barbosa, R. Barros, J. Maciel, M.C.L. Martins, R.M. Gonçalves, M.A. Barbosa, Adsorbed fibrinogen leads to improved bone regeneration and correlates with differences in the systemic immune response, Acta Biomater. 9 (7) (2013) 7209–7217, https://doi.org/10.1016/j.actbio.2013.04.008.
[70] J. Maciel, M. Oliveira, E. Colton, A. McNally, C. Oliveira, J. Anderson, M. Barbosa, Adsorbed fibrinogen enhances production of bone- and angiogenic-related factors by monocytes/macrophages, Tissue Eng. A 20 (2014) 250–263, https://doi.org/10.1089/ten.TEA.2012.0439.
[71] K.E. Bräuer, K. Brockers, J. Moneer, A. Feuchtinger, E. Wollscheid-Lengeling, A. Lengeling, A. Wolf, Phylogenetic and genomic analyses of the ribosomal oxygenases Riox1 (No66) and Riox2 (Mina53) provide new insights into their evolution, BMC Evol. Biol. 18 (1) (2018) 96, https://doi.org/10.1186/s12862-018-1215-0.
[72] L. Yu, Q. Tu, Q. Han, L. Zhang, L. Sui, L. Zheng, S. Meng, Y. Tang, D. Xuan, J. Zhang, D. Murray, Q. Shen, J. Cheng, S.H. Kim, L.Q. Dong, P. Valverde, X. Cao, J. Chen, Adiponectin regulates bone marrow mesenchymal stem cell niche through a unique signal transduction pathway: an approach for treating bone disease in diabetes, Stem Cell. 33 (1) (2015) 240–252, https://doi.org/10.1002/stem.1844.
[73] S. Yang, H. Liu, Y. Liu, L. Liu, W. Zhang, E. Luo, Effect of adiponectin secreted from adipose-derived stem cells on bone-fat balance and bone defect healing, J. Tissue Eng. Regen. Med. 13 (11) (2019) 2055–2066, https://doi.org/10.1002/term.2915.
[74] Z. Hamidouche, O. Fromigué, J. Ringe, T. Häupl, P.J. Marie, Crosstalks between integrin alpha 5 and IGF2/IGFBP2 signalling trigger human bone marrow-derived mesenchymal stromal osteogenic differentiation, BMC Cell Biol. 11 (44) (2010), https://doi.org/10.1186/1471-2121-11-44.
[75] R.K. Globus, S.B. Doty, J.C. Lull, E. Holmuhamedov, M.J. Humphries, C.H. Damsky, Fibronectin is a survival factor for differentiated osteoblasts, J. Cell Sci. 111 (10) (1998) 1385–1393, https://doi.org/10.1242/jcs.111.10.1385.
[76] C. Thouverey, J. Caverzasio, Focus on the p38 MAPK signaling pathway in bone development and maintenance, BoneKEy Rep. 4 (711) (2015), https://doi.org/10.3389/fcell.2016.00040.
[77] M. Vermeren, R. Lyraki, S. Wani, R. Airik, O. Albagha, R. Mort, F. Hildebrandt, T. Hurd, Osteoclast stimulation factor 1 (Ostf1) KNOCKOUT increases trabecular bone mass in mice, Mamm. Genome 28 (11–12) (2017) 498–514, https://doi.org/10.1007/s00335-017-9718-3.
[78] J. Zhang, Z. Ma, K. Yan, Y. Wang, Y. Yang, X. Wu, Matrix gla protein promotes the bone formation by up-regulating Wnt/β-catenin signaling pathway, Front. Endocrinol. 10 (2019) 891, https://doi.org/10.3389/fendo.2019.00891.
[79] P.S. Sharif, M. Abdollahi, The role of platelets in bone remodeling, Inflamm. Allergy - Drug Targets 9 (5) (2010) 393–399, https://doi.org/10.2174/187152810793938044.
[80] M. Kawai, C.J. Rosen, The insulin-like growth factor system in bone: basic and clinical implications, Endocrinol Metab. Clin. N. Am. 41 (2) (2012) 323–333, https://doi.org/10.1016/j.ecl.2012.04.013.
[81] S. Cazalbou, C. Combes, D. Eichert, C. Rey, M. Glimcher, Poorly crystalline apatites: evolution and maturation in vitro and in vivo, J. Bone Miner. Metabol. 22 (2004) 310–317, https://doi.org/10.1007/s00774-004-0488-0.
[82] N. Vandecandelaere, C. Rey, C. Drouet, Biomimetic apatite-based biomaterials: on the critical impact of synthesis and post-synthesis parameters, J. Mater. Sci. Mater. Med. 23 (2012) 2593–2606, https://doi.org/10.1007/s10856-012-4719-y.
[83] C. Rey, C. Combes, C. Drouet, H. Sfihi, Chemical diversity of apatites, Adv. Sci. Technol. 49 (2006) 27–36, https://doi.org/10.4028/www.scientific.net/AST.49.27.
[84] S. Cazalbou, C. Combes, D. Eichert, C. Rey, Adaptative physico-chemistry of bio-related calcium phosphates, J. Mater. Chem. 14 (2004) 2148–2153, https://doi.org/10.1039/B401318B.
[85] J.M. Sadowska, J. Guillem-Marti, M.-P. Ginebra, The influence of physicochemical prop- erties of biomimetic hydroxyapatite on the in vitro behavior of endothelial progenitor cells and their interaction with mesenchymal stem cells, Adv. Healthc. Mater. 8 (2) (2019) 1801138, https://doi.org/10.1002/adhm.201801138.
[86] F. Barrère, C.M. van der Valk, R.A.J. Dalmeijer, C.A. van Blitterswijk, K. de Groot, P. Layrolle, In vitro and in vivo degradation of biomimetic octacalcium phosphate and carbonate apatite coatings on titanium implants, J. Biomed. Mater. Res. A 64A (2) (2003) 378–387, https://doi.org/10.1002/jbm.a.10291.
[87] C. Botelho, R. Brooks, M. Kanitakahara, C. Ohtsuki, S. Best, M. Lopers, N. Rushton, W. Bonfield, J. Santos, Effect of protein adsorption onto the dissolution of silicon-substituted hydroxyapatite, J. Encapsulation Adsorpt. Sci. 1 (4) (2011) 72–79, https://doi.org/10.4236/jeas.2011.14010.
[88] M. Nieuwoudt, R. Shahlori, D. Naot, R. Patel, H. Holtkamp, C. Aguergaray, M. Watson, D. Musson, C. Brown, N. Dalbeth, J. Cornish, C. Simpson, Raman spectroscopy reveals age- and sex-related differences in cortical bone from people with osteoarthritis, Sci. Rep. 10 (2020) 19443, https://doi.org/10.1038/s41598-020-76337-2.
[89] M. Toledano, E. Osorio, F.S. Aguilera, I. Cabello, M. Toledano-Osorio, R. Osorio, Ex vivo detection and characterization of remineralized carious dentin, by nanoindentation and single point Raman spectroscopy, after amalgam restoration, J. Raman Spectrosc. 48 (3) (2017) 384–392, https://doi.org/10.1002/jrs.5055.
[90] S. Cazalbou, D. Eichert, X. Ranz, C. Drouet, C. Combes, M. Harmand, C. Rey, Ion exchanges in apatites for biomedical application, J. Mater. Sci. Mater. Med. 16 (5) (2005) 405–409, https://doi.org/10.1007/s10856-005-6979-2.
[91] C. Drouet, J. Gómez-Morales, M. Iafisco, S. Sarda, Calcium Phosphate Surface Tailoring Technologies for Drug Delivering and Tissue Engineering and Applied Aspects, 2012, https://doi.org/10.2174/978160805462611201010043.
[92] S. Von Euw, Y. Wang, G. Laurent, C. Drouet, F. Babonneau, N. Nassif, T. Azaïs, Bone mineral: new insights into its chemical composition, Sci. Rep. 9 (2019) 8456, https://doi.org/10.1038/s41598-019-44620-6.
[93] K. Wang, M. Wang, Q. Wang, X. Lu, X. Zhang, Computer simulation of proteins adsorption on hydroxyapatite surfaces with calcium phosphate ions, J. Eur. Ceram. Soc. 37 (6) (2017) 2509–2520, https://doi.org/10.1016/j.jeurceramsoc.2017.02.013.
[94] M. Espanol, G. Mestres, T. Luxbacher, J.-B. Dory, M.-P. Ginebra, Impact of porosity and electrolyte composition on the surface charge of hydroxyapatite biomaterials, ACS Appl. Mater. Interfaces 8 (1) (2016) 908–917, https://doi.org/10.1021/acsami.5b10404.
[95] M. Espanol, I. Casals, S. Lamtahri, M.-T. Valderas, M.-P. Ginebra, Assessment of protein entrapment in hydroxyapatite scaffolds by size exclusion chromatography, Biointerphases 7 (37) (2012), https://doi.org/10.1007/s13758-012-0037-7.
[96] R.A. Hartvig, M. van de Weert, J. Østergaard, L. Jorgensen, H. Jensen, Protein adsorption at charged surfaces: the role of electrostatic interactions and interfacial charge regulation, Langmuir 27 (6) (2011) 2634–2643, https://doi.org/10.1021/la104720n.
[97] D.M. Vasconcelos, R.M. Gonçalves, C.R. Almeida, I.O. Pereira, M.I. Oliveira, N. Neves, A.M. Silva, A.C. Ribeiro, C. Cunha, A.R. Almeida, C.C. Ribeiro, A.M. Gil, E. Seebach, K.L. Kynast, W. Richter, M. Lamghari, S.G. Santos, M.A. Barbosa, Fibrinogen scaffolds with immunomodulatory properties promote in vivo bone regeneration, Biomaterials 111 (2016) 163–178, https://doi.org/10.1016/j.biomaterials.2016.10.004.
[98] I. Blumenfeld, S. Srouji, Y. Lanir, D. Laufer, E. Livne, Enhancement of bone defect healing in old rats by TGF-β and IGF-1, Exp. Gerontol. 37 (4) (2002) 553–565, https://doi.org/10.1016/S0531-5565(01)00215-7.
[99] A.I. Caplan, D. Correa, PDGF in bone formation and regeneration: new insights into a novel mechanism involving MSCs, J. Orthop. Res. 29 (12) (2011) 1795–1803, https://doi.org/10.1002/jor.21462.
[100] H.T. Shiu, B. Goss, C. Lutton, R. Crawford, Y. Xiao, Formation of blood clot on biomaterial implants influences bone healing, Tissue Eng. B Rev. 20 (6) (2014) 697–712, https://doi.org/10.1089/ten.teb.2013.0709.
[101] R.E. Marx, E.R. Carlson, R.M. Eichstaedt, S.R. Schimmele, J.E. Strauss, K.R. Georgeff, Platelet-rich plasma: growth factor enhancement for bone grafts, Oral Surg, Oral Med. Oral Pathol. Oral Radiol. Endodontol. 85 (6) (1998) 638–646, https://doi.org/10.1016/S1079-2104(98)90029-4.

[102] I. Martineau, E. Lacoste, G. Gagnon, Effects of calcium and thrombin on growth factor release from platelet concentrates: kinetics and regulation of endothelial cell proliferation, Biomaterials 25 (18) (2004) 4489–4502, https://doi.org/10.1016/j.biomaterials.2003.11.013.

[103] L.R. Kark, J.M. Karp, J.E. Davies, Platelet release increases the proliferation and migration of bone marrow-derived cells cultured under osteogenic conditions, Clin. Oral Implants Res. 17 (3) (2006) 321–327, https://doi.org/10.1111/j.1600-0501.2005.01189.x.

[104] J. Beattie, H. Al-Khafaji, P.R. Noer, H.E. Alkharobi, A. Alhodhodi, J. Meade, R. El-Gendy, C. Oxvig, Insulin-like growth factor-binding protein action in bone tissue: a key role for pregnancy- associated plasma protein-A, Front. Endocrinol. 9 (2018) 31, https://doi.org/10.3389/fendo.2018.00031.

[105] M. Dixit, S.B. Poudel, S. Yakar, Effects of GH/IGF axis on bone and cartilage, Mol. Cell. Endocrinol. 519 (2021) 111052, https://doi.org/10.1016/j.mce.2020.111052.

[106] L. Chen, W. Jiang, J. Huang, B.-C. He, G.-W. Zuo, W. Zhang, Q. Luo, Q. Shi, B.-Q. Zhang, E.R. Wagner, J. Luo, M. Tang, C. Wietholt, X. Luo, Y. Bi, Y. Su, B. Liu, S.H. Kim, C.J. He, Y. Hu, J. Shen, F. Rastegar, E. Huang, Y. Gao, J.-L. Gao, J.-Z. Zhou, R.R. Reid, H.H. Luu, R.C. Haydon, T.-C. He, Z.-L. Deng, Insulin-like growth factor 2 (IGF-2) potentiates BMP-9-induced osteogenic differentiation and bone formation, J. Bone Miner. Res. 25 (11) (2010) 2447–2459, https://doi.org/10.1002/jbmr.133.